Novel Modular Electrocatalytic Processing for Simultaneous Conversion of Carbon Dioxide and Wet Shale Gas into Valuable Products

Final Technical Report

DOE Cooperative Agreement No. DE-FE0031709

Project PI: Jason Trembly
Phone: (740) 566-7046
E-mail: trembly@ohio.edu

Project Period:
October 1, 2018 through June 30, 2022

Prepared by:
Ahmad Abu Hajer, Andrew Kasick, Samgopiraj Velraj, Damilola Daramola, and Jason Trembly

Submitted by:
Ohio University
1 Ohio University
Athens, OH 45701

Submitted to:
U.S. Department of Energy
Office of Fossil Energy and Carbon Management
National Energy Technology Laboratory

Disclaimer

Acknowledgement

This material is based upon work supported by the Department of Energy National Energy Technology Laboratory under award Number DE-FE0031709.

Abstract

This report examines solid oxide electrolyzer cell (SOEC) technology as an alternative process for the manufacture of carbon monoxide (CO) and the separation of ethane (C_2H_6) from wet natural gas (WNG). SOEC cathodes for the electrochemical reduction of carbon dioxide (CO_2) to CO and SOEC anodes for the selective electrochemical oxidation of C_2H_6 to ethylene (C_2H_4) are described and presented. Lifecycle and techno-economic analyses (LCA and TEA) utilizing SOEC technology for the production of CO are also reported.

Table of Contents

1. Introduction

The primary goal of the National Energy Technology Laboratory (NETL)'s Carbon Use and Reuse program is the development of cost-effective technologies which convert CO_2 into valuable products offering a more sustainable carbon lifecycle over conventional methods. The first step towards developing CO_2 reuse technologies is to identify methods compatible with the current energy infrastructure and offering synergisms between two or more energy sectors. This project attempts to develop an intermediate temperature SOEC technology that simultaneously converts CO_2 into CO and separates C_2H_6 from WNG using electric power, which offers lower CO_2 lifecycle emissions when compared to the current conventional cryogenic separation pathways.

1.1. Carbon Monoxide Production

CO is an important industrial gas used in manufacturing bulk chemicals. The vast majority of CO (>90%), is converted into chemicals such as methanol when in the form of syngas with hydrogen (H_2). However, industrial gas suppliers including Praxair, Linde, Air Liquide and Air Products, competitively produce bulk CO for the chemical industry. Although public information regarding the bulk U.S. CO market is limited, OHIO estimates major industrial gas suppliers generate 300-400 MMscf/day CO with an annual market value of $1.24-1.66 billion. Bulk CO is used in the production of several important chemical precursors such as phosgene and commodity materials via carbonylation including aldehydes, ketones, carboxylic acids, anhydrides, esters, amides, imides, carbonates, ureas, and isocynanates. Further, high purity CO (>99.99%) is used in electronics manufacturing. Further growth of the bulk CO market is expected as a significant amount of chemical manufacturing returns to the U.S. due to low hydrocarbon pricing from unconventional gas reservoirs. As CO production costs are highly sensitive to capital costs, most commercial CO production facilities have production capacities greater than 5 MMscf/day. CO manufacturing in the U.S. consumes upwards of 200 billion standard cubic feet of natural gas annually.

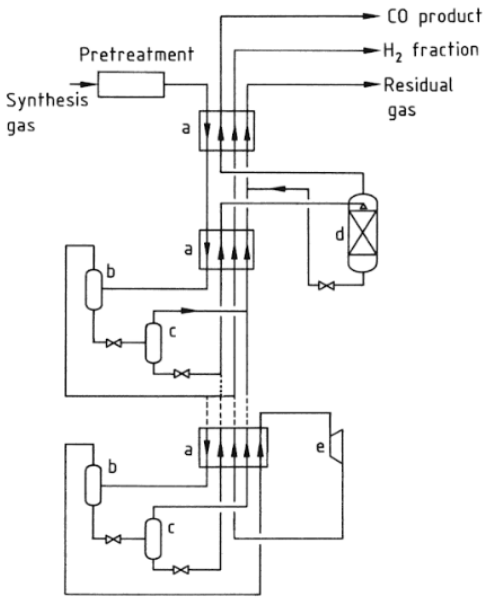

Figure 1. Bulk CO Production Using Cryogenic Partial Condensation Process [1]. Permission Provided by Wiley-VCH.

Industrial bulk CO is produced by separating CO from syngas (containing H_2) typically generated via steam methane reforming (SMR) using natural gas as the feedstock. Various separation technologies are used including cryogenic separation (i.e. cold box), pressure swing adsorption (PSA), membrane separation, and ammonium salt solution absorption. Design of the system is highly dependent upon feed gas composition and typically natural gas containing <1 vol.% nitrogen (N_2) is used. Some limited use of membrane separation is used in facilities producing <0.5 MMscf/day CO. However, as CO production cost is highly dependent upon process capital (80-85%), larger production facilities >5 MMscf/day are preferred [2]. The cold box process, shown in Figure 1, causes partial condensation of CO from H_2 at cryogenic conditions. This process typically generates bulk CO (98-99%) and H_2 (97-98%) products. Before undergoing cryogenic separation, the CO-containing feed

gas is first treated to remove CO_2 and water (H_2O). The feed gas is compressed to pressures (24-35 bar) which allow temperatures to be reached to cause partial condensation of CO (-130 to 106 °C). The cryogenic partial condensation cycle consists of flashing and heat exchange which yields a CO product from the CO/CH_4 splitter [1,3]. The compression/expansion and high degree of heat integration required for this process make it capital intensive with CO pricing sensitive or process scale. If greater CO purity is desired, a liquid methane (CH_4) wash unit operating at -180 °C is used [1,3].

1.2. Natural Gas Liquids Separation

C_2H_6 and other natural gas liquids (NGLs) are separated from natural gas (i.e. CH_4) via a turbo-expansion process (Figure 2a) combined with external refrigerant to recover approximately 80% of C_2H_6 contained in natural gas. This processing is particularly important for WNG to prepare it for transport in interstate pipelines. First, the raw natural gas is compressed and treated to remove acid gases (H_2S, CO_2, etc.), typically via a monoethanolamine (MEA)-based absorption unit to produce the sweet gas, which is then dehydrated using triethylene glycol (TEG). Following dehydration, the gas enters a cryogenic separation unit where NGLs are recovered. Cryogenic separation is accomplished via heat integration and expansion of the gas causing its temperature to reach -90 °C, before entering the demethanizer. In the demethanizer, a bottom liquid NGL stream (C_{2+} mixture) and top CH_4-rich stream are produced. If further separation of the liquid NGL stream is desired, a fractionation train (Figure 2b) is used in generating separate C_2H_6, propane (C_3H_8), and C_3 streams.

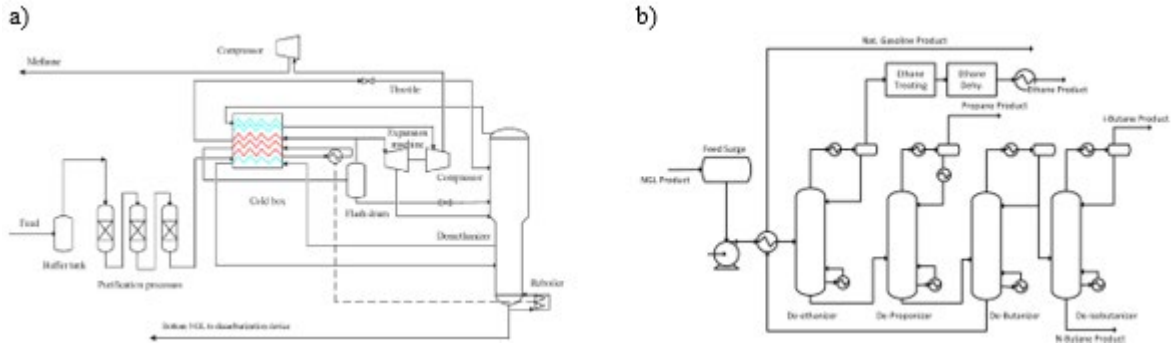

Figure 2. a) Turbo-expander process for C2+ separation from CH4 (Permission provided by Elsevier.) and b) NGL fractionation train.

1.3. Project Objectives

The overall objective of this project is to develop a process which simultaneously converts CO_2 and NGLs (mainly C_2H_6) in WNG into valuable CO and chemicals/fuels respectively, using electrical energy. The primary objective of Phase I is to identify an intermediate temperature SOEC process configuration that offers the technical feasibility of producing CO and removing C_2H_6 from WNG at costs equivalent to current commercial processes, with significant reduction in lifecycle CO_2 emissions over conventional processes.

2. CO_2 Electrolysis by Means of Transition Metals and Alloy electrocatalysts

High temperature CO_2 electrolysis using solid oxide cells (SOCs) has shown to be an attractive option for CO production due to its high efficiency and enhanced reaction kinetics [4]. Research related to CO_2 reduction in SOECs has been mainly focused on using perovskites and composite perovskite-fluorites to replace the state of art Ni-YSZ cathodes. Hence, not much attention was drawn towards using catalytically active cathodes such as gadolinium doped ceria (GDC) to replace yttria-stabilized zirconia (YSZ) in SOECs. Also, few studies have investigated the catalytic activity of other transition metals toward CO_2 reduction in SOECs. A thorough literature review has shown that gadolinium doped ceria (GDC) enhanced the high temperature CO_2 electrolysis due to the reduction of cerium (Ce) from Ce^{4+} to Ce^{3+} which facilitated oxygen vacancy formation and helped with the adsorption of CO_2 and desorption of CO [5]. Moreover, first principles studies using density functional theory (DFT) indicated that transition metals such as cobalt (Co), nickel (Ni), iron (Fe), and ruthenium (Ru) are best suited electrocatalysts for high temperature CO_2 electrolysis [6].

This chapter discusses the CO_2 electroreduction performance of in-house fabricated SOCs having GDC cathodes infiltrated with different transition metal based electrocatalysts such as Co, Ni, Cu, and Co-Ni alloys. The electrochemical performance of the best identified catalyst was also assessed under flue gas operating conditions.

2.1. Experimental Methodologies

2.1.1. *Cell Fabrication*

Electrochemical experiments were performed using electrolyte-supported button cells that have a diameter of 25 mm. The cell design consisted of a scandia-stabilized zirconia (ScSZ) substrate as an electrolyte, a porous $Gd_{0.1}Ce_{0.9}O_{1.95}$ (GDC 10) cathode, and a $(La_{0.8}Sr_{0.2})_{0.95}MnO_{3-x}$ (LSM20) based anode. To ensure the quality and repeatability of the experimental results, the electrolyte substrates and the powders used in electrodes fabrication were purchased from Fuelcellmaterials (Columbus, OH).

The powder used in fabricating the porous cathode structure was composed of 80 wt.% GDC10 and 20 wt.% graphite (Part no: 47275, Alfa Aesar). The mixture was prepared by ball milling appropriate amounts of GDC10 and graphite along with ethanol and triton x-100 (part no: 2315025, Sigma Aldrich) surfactant at a rotational speed of 60 rpm for 15 hours. The liquid slurry was then dried for 24 hours at 110 °C using an oven and the resulting powder was used in fabricating the cathode of the CO_2 reduction cell. When fabricating the SOECs, two GDC10 base layers were initially screen printed on each electrolyte side. These layers provided strong adhesion between the electrodes and the electrolyte substrate [7]. Also, they acted as buffer layers that minimized the chemical interactions between both electrodes' components and the electrolyte substrate [8]. After sintering the GDC10 interlayers, six layers of the cathode powder were screen printed on top of the GDC10 layers on one side of the electrolyte and were then sintered at 1300 °C for 10 hours to create a porous scaffold structure. Lastly, six layers of LSM20 based anodes were screen printed on top of the GDC10 interlayers on the other side of the electrolyte and were then sintered at 1200 °C for 5 hours in air. Since the screen used for fabricating both electrodes had an opening diameter equal to 1.78 cm, the resulting surface areas for both electrodes was equal to 2.48 cm^2. A schematic diagram of the electrolyte supported button cells used in CO_2 electroreduction experiments is shown in Figure 3.

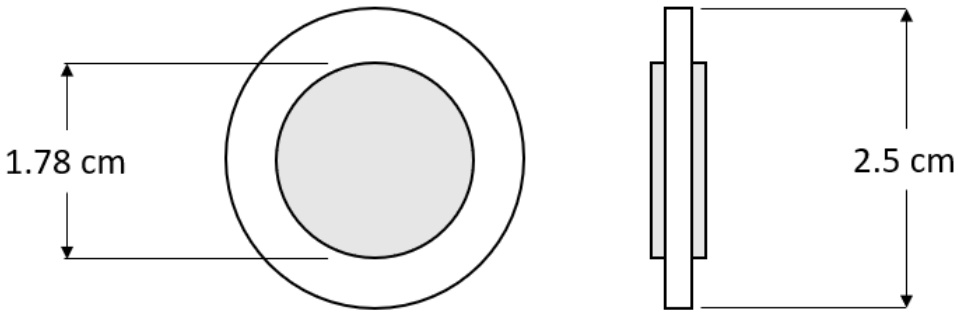

Figure 3. A schematic of button cells used for testing.

Transition metal electrocatalysts were added into the cathode scaffold structure using a liquid infiltration method. The infiltrate precursor solutions were prepared by mixing 8.33 ml of a 3 M transition metal nitrate solution, 4.17 ml deionized (DI) water, 0.28 ml of triton x-100 surfactant, and 12.43 ml of ethanol in a 25 ml volumetric flask. For the Co-Ni alloyed electrocatalysts infiltration, 0.961 g of citric acid was added as a chelating agent to the infiltrate solution to ensure better interaction between metal cations and thus result in alloy formation during CO_2 electroreduction testing. The infiltrate solution was transferred into the cathode's scaffold structure in aliquots of 15 μl using a micropipette. After each infiltration cycle, the infiltrated cell was put under vacuum to ensure even distribution of the infiltrate solution throughout the scaffold structure. The cell was then placed on a hot plate that was set at 450 °C to decompose the nitrates. The infiltration process was repeated until the weight of the infiltrated catalyst formed about 33-35% of the total cathode's weight. The infiltrated cell was then calcined in air at 900 °C for 3 hours.

2.1.2. *Materials Characterization*

X-ray diffractometry (XRD) was conducted on infiltrated cathodes using a benchtop diffractometer (miniflex, Rigaku) with a Cu-Kα1 source at a wavelength of 1.54059 Å. The XRD patterns were analyzed using PDXL-2 software to identify the phases of the infiltrated catalysts. The cross-section of the CO_2 reduction cells was examined using a scanning electron microscope (SEM) (model: JSM-63909, Jeol). Moreover, the stoichiometric composition for the alloyed metal electrocatalysts was analyzed using an energy dispersive spectrometer (EDS) attached to the SEM.

2.1.3. *Electrochemical Testing*

The CO_2 reduction cell was sealed to an alumina tube using a composite glass-ceramic sealant (part number: GL-1862, Mo-sci) in a way that the cathode side of the cell was facing the inside of the alumina tube and the anode side was facing the atmosphere. Silver wire meshes were used as current collectors and were fitted on both sides of the CO_2 reduction cell using conductive silver paint (part number: 05002-AB, SPI supplies). Leads from both current collectors were connected to a potentiostat (model: Interface 5000P, Gamry) using a four-probe connection method with the working and working sense leads connected to the cathode while the counter along with the reference leads connected to the anode side of the cell .The test fixture was placed inside a high temperature tube furnace (model: Lindberg/Blue M, Thermo Fisher Scientific, USA) and was subjected to a temperature program to cure the sealant and

maintain the designated testing temperature. Three testing temperatures were used during this study: 750, 800, and 850 °C.

When reaching the testing temperature, argon (Ar) was flown inside the fixture at a flow rate of 50 sccm while air was flown at a rate of 200 sccm near the anode side of the cell. The exhaust stream from the cathode side of the cell was then analyzed using a gas chromatograph (GC) (model: Micro GC Fusion, Inficon) to detect any leaks within the test fixture. After confirming that the fixture had no leaks, 10 vol.% H_2 balanced Ar was passed through the cathode side at a flow rate of 50 sccm for approximately 2 hours to reduce the metal infiltrated catalyst from its oxide form. CO_2 electroreduction tests were then initiated by flowing 81 vol.% CO_2, 10 vol.% CO, and 9 vol.% N_2 on the cathode side while maintaining the air flow rate at 200 sccm on the anode side. After achieving stable open circuit voltage (OCV) readings, polarization curves and electrochemical impedance spectroscopy (EIS) data were obtained. The EIS data was recorded under OCV with an AC amplitude of 10 mV over the frequency range from 100 kHz to 12.59 mHz. After obtaining polarization curves, the cells were galvanostatically tested at 0.1, 0.2, 0.3, and 0.4 $A \cdot cm^{-2}$ while the exhaust gas from the cathode side was analyzed using the GC at each current density to determine the Faradaic efficiency and the CO production rates.

2.1.4. *Flue Gas Testing*

A Co infiltrated cell was tested at 800 °C using the gas composition shown in Table 1. The shown composition was believed to mimic the flue gas mixture exiting from a flue gas desulfurization unit (FGD) in a coal fired power plant.

Table 1. Flue gas composition.

Gas species	Vol.%
O_2	1.84
N_2	51.4
CO_2	30.1
H_2O	16.7
SO_2	0.0002

When reaching the testing temperature, Air was flown near the anode side of the cell at a flow rate of 200 sccm, while 80 sccm of 10 vol.% H_2 balanced with Ar was flown onto the cathode side of the cell for one hour to reduce the metal electrocatalyst from its oxide form. 80 sccm of dry flue gas mixture composed of 60.8 vol.% N_2, 2.175 vol.% oxygen(O_2), 37 vol.% CO_2, and 2.5 ppm Sulfur dioxide (SO_2) was then flown through a humidifier bottle which was connected to the cathode side of the cell's fixture. The humidifier bottle was set at 56.5 °C to provide the cell with the adequate moisture content and to obtain the flue gas concentrations mentioned in Table 1. Electrochemical testing was initiated after achieving stable open circuit potential (OCP) values. The cell was galvanostatically tested by subjecting it to a constant current density of 0.4 $A \cdot cm^{-2}$ for 34 hours.

2.2. Results

2.2.1. *Microstructure and Characterization of Fabricated Cells*

Figure 4 (a) shows the cross-sectional view of a fabricated cell composed of an ScSZ based substrate, a transition metal infiltrated GDC scaffold, and an LSM 20 based anode. In Figure 4 (a and b) it is apparent that the cathode structure has good porosity, and both electrodes are well adhered to the electrolyte

surface. Also, EDS maps shown in Figure 4 (c and d) indicate that the catalyst particles form a continuous coating over the scaffold structure thus extending the surface area of the triple phase boundary (TPB) sites throughout the electrode structure. XRD Patterns shown in Figure 4 (e) indicate the formation of tricobalt tetroxide (Co_3O_4) (PDF #: 00-042-1467), cupric oxide (CuO) (PDF #: 01-073-6023), and nickel oxide (NiO) (PDF #: 01-078-4376) after calcining the cells infiltrated with Co, Cu, and Ni nitrates, respectively. Moreover, XRD patterns indicate that no solid-state reactions have occurred between the infiltrated electrocatalysts and GDC10 scaffold during the calcination process.

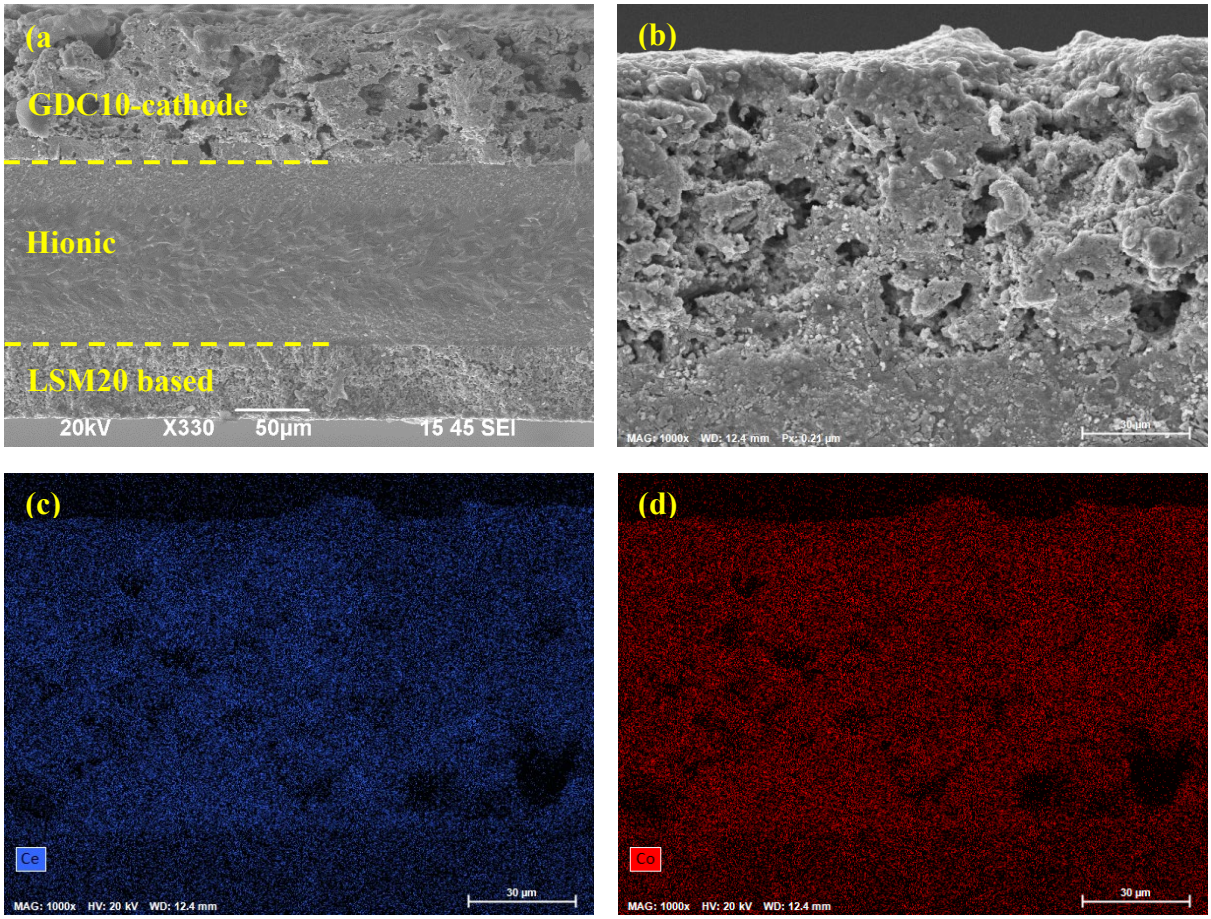

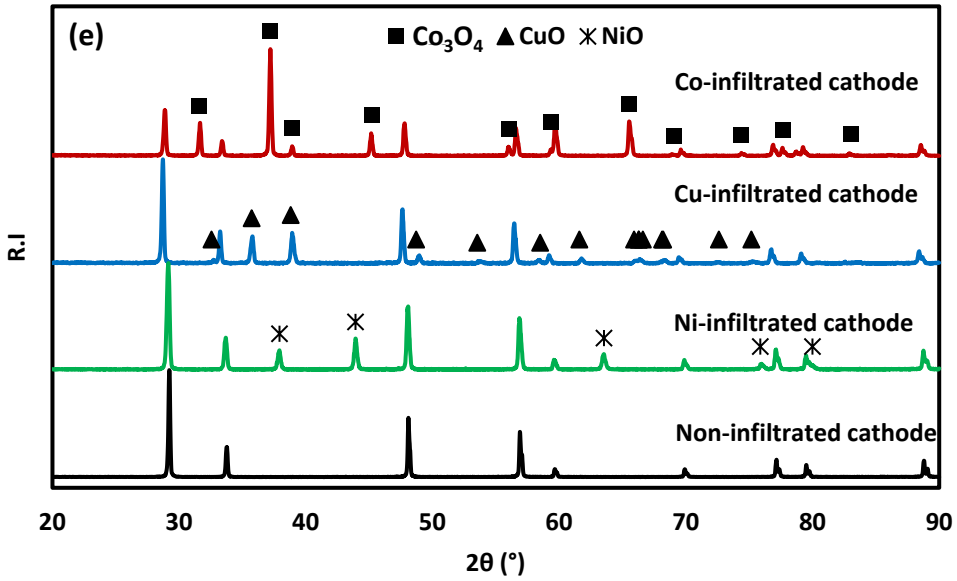

Figure 4. (a) Cross sectional SEM image of a CO_2 electroreduction cell; (b) Zoomed-in SEM image for the infiltrated GDC scaffold; (c) EDS map for cerium; (d) EDS map for cobalt; (e) XRD patterns for GDC-10 infiltrated cathodes calcined at 900 °C for 3 hours.

Figure 5 (a) shows a zoomed-in view of a GDC scaffold infiltrated with Ni-Co alloy electrocatalyst using a Co:Ni ratio of 1:3. According to the EDS mapping results shown in Figure 5 (b), the Co:Ni stoichiometric ratio was 1:2.84 which is close to the stoichiometric ratio of the catalysts present in the precursor solution infiltrated into the GDC scaffold before calcination. Moreover, EDS maps shown in Figure 5 (c and d) indicate that the infiltrated catalyst particles form a continuous coating throughout the scaffold structure which helps in extending the TPB sites throughout the electrode structure. As shown in Figure 5 (e), the XRD Patterns of the cathodes infiltrated with Ni-Co alloy electrocatalysts indicated the formation of Co_3O_4 (PDF #: 00-042-1467) and NiO (PDF #: 01-078-4376) solid solutions after calcining the cells at 900 °C for 3 hours. The formed solid solutions are believed to form Ni-Co alloys at desired ratios when subjected to a reducing gas such as H_2 according to Kuboon, et al. [9].

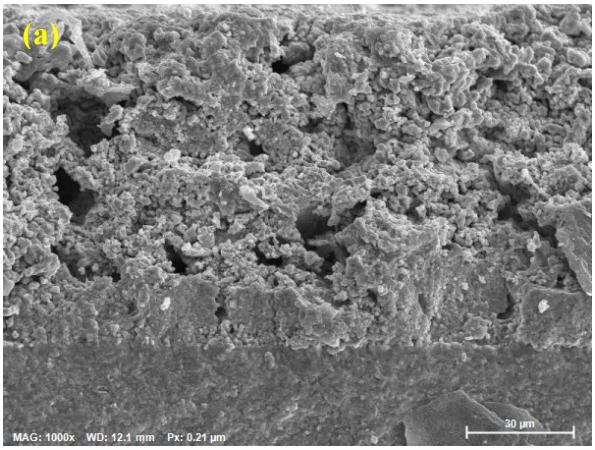

(b)

Element	At. No.	Mass [%]	Mass Norm. [%]	Atom [%]	abs. error [%] (3 sigma)
Sc	21	0.99	1.08	2.26	0.12
Co	27	3.95	4.30	6.84	0.35
Ni	28	11.17	12.18	19.44	0.92
Zr	40	25.95	28.29	29.06	2.97
Pd	46	27.48	29.96	26.37	2.64
Ce	58	20.33	22.16	14.82	1.68
Gd	64	1.85	2.02	1.20	0.26
		91.72	**100.00**	**100.00**	

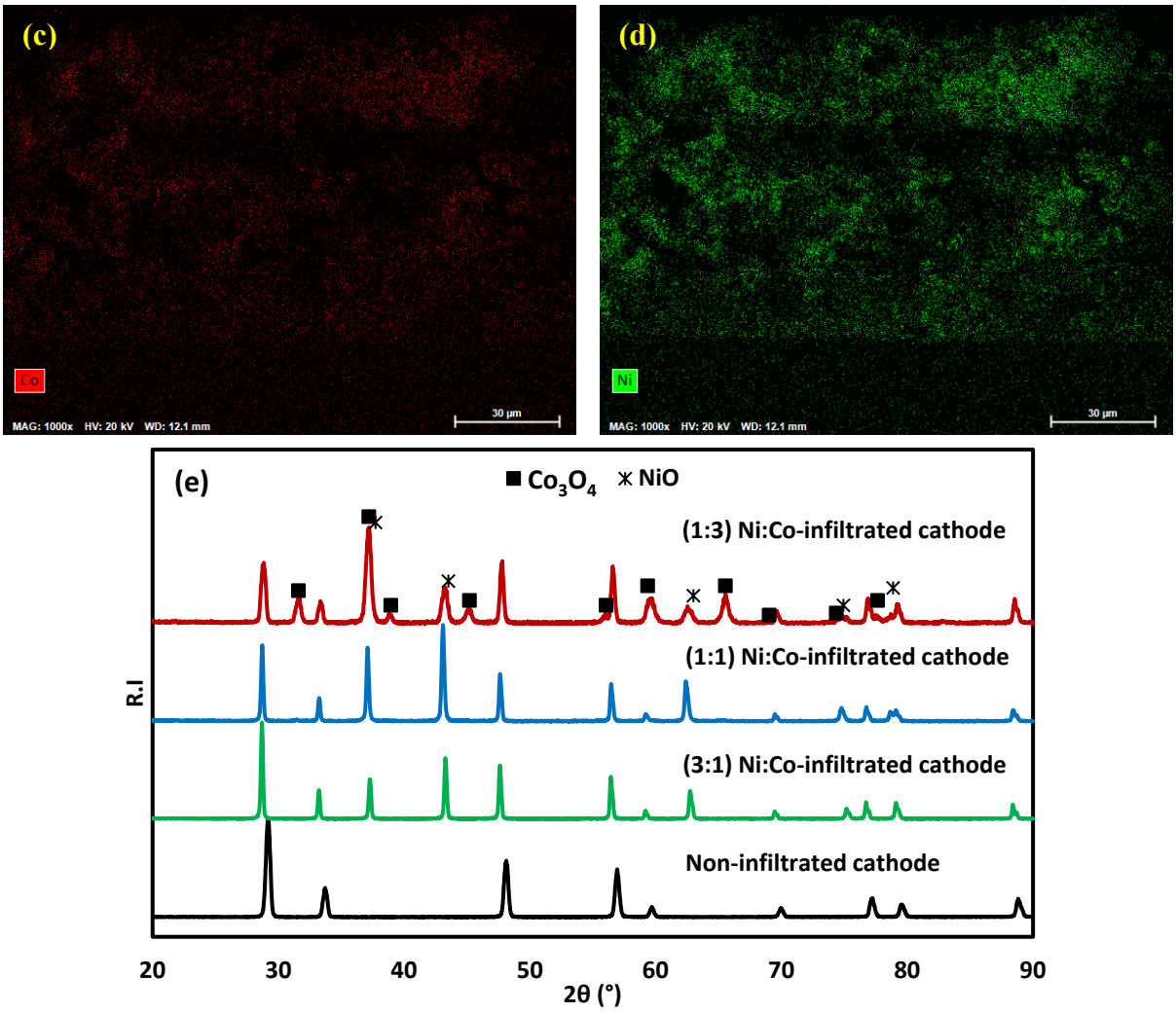

Figure 5. (a) Zoomed-in SEM for a GDC scaffold infiltrated with 3:1 Ni:Co; (b) EDS mapping results; (c) EDS map for cobalt; (d) EDS map for nickel; (e) XRD patterns for non-infiltrated and Ni-Co infiltrated GDC-10 cathodes calcined at 900 °C for 3 hours.

2.2.2. *Electrocatalysts Oxidation Analysis*

The reactant gas introduced into the cathode side has CO in its composition to keep the metal electrocatalysts from oxidation during the electroreduction experiments. To ensure that oxidation is unlikely to occur during testing, thermodynamic calculations performed with HSC 6.1 software were used to evaluate the activity of the metal oxide phases that are likely to form at the different testing temperatures. Equations (**1** and (**2**) show the oxidation reaction of transition metals when reacting with CO_2 gas, and the difference in Gibbs free energy for this reaction, respectively.

$$M + CO_{2(g)} \rightarrow MO + CO_{(g)} \quad (1)$$

$$dG_{ox} = -RT * ln\left(\frac{a_{MO} * a_{CO}}{a_M * a_{CO_2}}\right) \quad (2)$$

Where M is transition metal, MO is transition metal oxide, dG_{ox} is the difference in Gibbs free energy for the metal oxidation reaction using CO_2, R is the universal gas constant, and T is the temperature. From equation (2), a negative value for $ln(a_{MO})$ means that oxidation is unlikely to happen. Figure 6 shows a plot of the calculated metal oxides activities versus temperature under the gas composition used for evaluating the CO_2 electroreduction performance of the tested transition metal electrocatalysts.

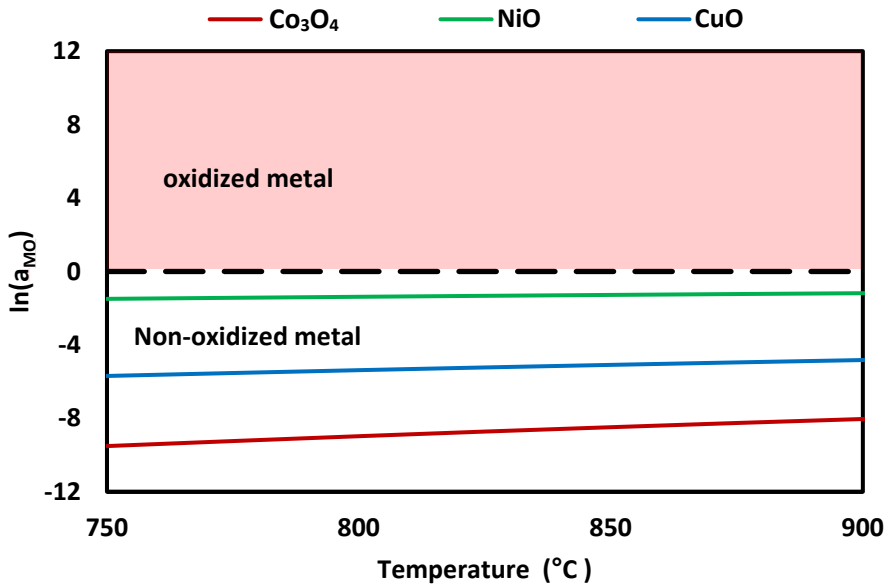

Figure 6. Metal oxide activity (aMO) versus temperature for a gas composition of 81 vol.% CO_2 - 10 vol.% CO – 9 vol.% N_2.

2.2.3. *Electrochemical Testing Results*

Figure 7 (a, c, and e) show the polarization curves for the cells tested at 750, 800, and 850 °C, respectively. It can be seen that the measured OCV values for the tested cells (equal to 0.873, 0.846, and 0.818 V when tested at 750, 800, and 850 °C, respectively) are close to the theoretical OCVs calculated using the Nernst equation (equal to 0.877, 0.848, and 0.819 V for 750, 800, and 850 °C, respectively) and are therefore indicative of a tightly sealed setup and accurate compositions of the gases delivered to both electrodes [10]. Cells with infiltrated transition metal electrocatalysts showed better electrochemical performance towards CO_2 electroreduction compared to the cells with non-infiltrated GDC scaffolds. Moreover, the performance of Cu infiltrated cells was better than the cells with non-infiltrated GDC scaffold, but was lower compared to the performance of Ni, Co, and Ni-Co infiltrated cells. The better electrochemical performance of Co, Ni, and Ni-Co alloys towards CO_2 electrolysis compared to Cu is due to their high oxygen binding energy (oxophilicity) as reported by Gu, et al. [6].

Figure 7 (b, d, and f) show the Nyquist plots for the cells tested at 750, 800, and 850 °C, respectively. The intercept of the Nyquist plots with the real axis at high frequency represents the ohmic resistance (R_s) of the tested cell which is mainly governed by the electrolyte material, electrolyte thickness, electrical contacts, and the electrode materials [11]. Moreover, the Nyquist plots of the tested cells represent two main electrochemical processes, a high frequency one mainly attributed to the charge transfer process for

CO_2 dissociation, and a low frequency one related to the mass transfer processes associated with the dissociative adsorption of CO_2 gas on the electrode surface and the subsequent diffusion of the active species to the charge transfer reaction sites [12,13].The difference between the intercept of the low frequency arc with the real axis and R_s represents the polarization resistance (R_p) of the tested cell which gives a clear indication of its electrochemical performance. R_p and R_s values for the tested cells are shown in Table 2.

Results obtained from the Nyquist plots indicate that the cells with transition metal infiltrated cathodes have lower R_s values compared to cells with non-infiltrated GDC cathodes which is attributed to the high electronic conductivity of the transition metal electrocatalysts. In addition to that, a decrease in R_s values was observed with the increase in testing temperatures owing to the improved ionic conductivity of the electrolyte substrate at higher operating temperatures [10]. The enhanced reaction kinetics at higher operating temperatures was reflected by an overall decrease in R_p values as the operating temperature increased for the tested cells [12,14].

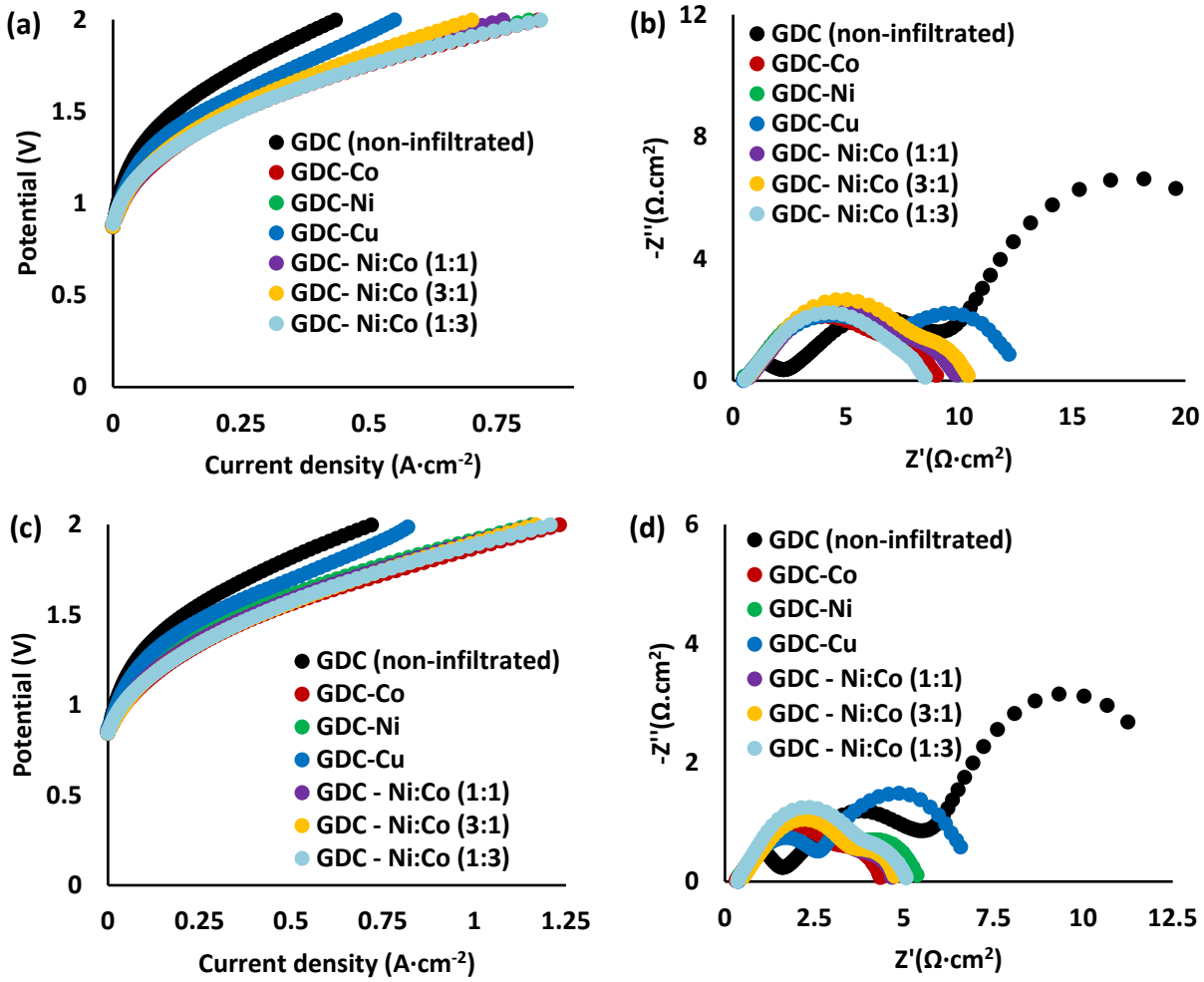

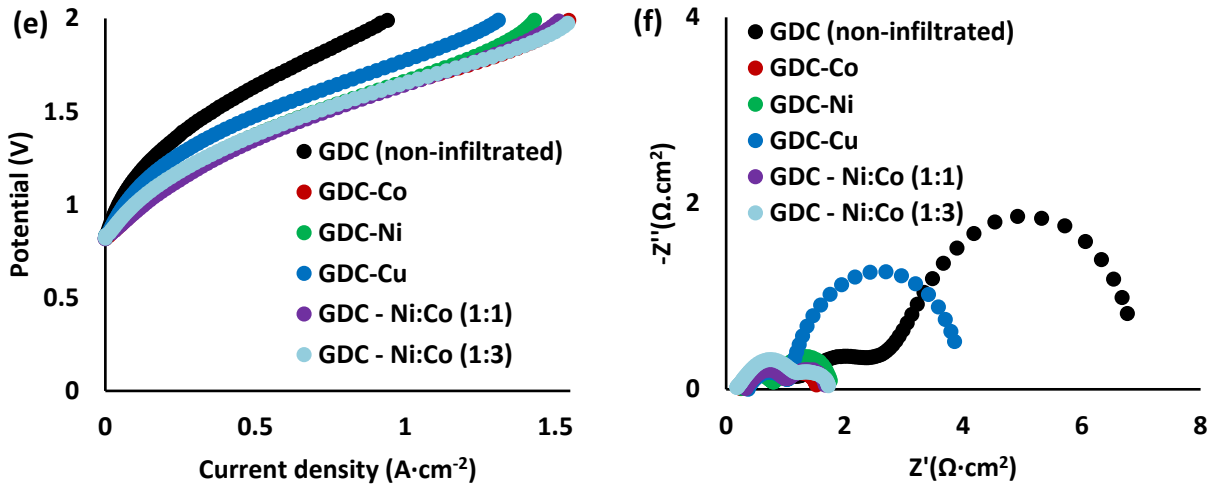

Figure 7. CO_2 electroreduction performance of tested SOECs: polarization curves at (a)750, (c) 800, and (e) 850 °C. Nyquist plots under OCV at (b) 750, (d) 800, and (f) 850 °C.

The CO_2 to CO conversions and faradaic efficiency for all the cells tested at 750, 800, and 850 °C are shown in Figure 8. No CO_2 conversion was observed for zero current density and the conversion increased linearly with increasing current densities. The cells had a faradaic efficiency > 95% at all applied current densities which indicated that little or no competing reactions other than CO_2 reduction had taken place.

Table 2. Results of EIS spectra for cells tested at different temperatures.

Temperature (°C)	Tested cell (Cathode composition)	R_s ($\Omega \cdot cm^2$)	R_p ($\Omega \cdot cm^2$)
750	GDC	2.14	22.13
	GDC-Co	0.46	8.54
	GDC-Ni	0.54	9.45
	GDC-Cu	0.46	11.57
	GDC- Ni:Co (1:1)	0.61	9.28
	GDC- Ni:Co (3:1)	0.53	9.87
	GDC- Ni:Co (1:3)	0.50	8.00
800	GDC	1.54	11.49
	GDC-Co	0.31	4.03
	GDC-Ni	0.47	4.93
	GDC-Cu	0.36	6.19
	GDC- Ni:Co (1:1)	0.37	4.30
	GDC- Ni:Co (3:1)	0.50	4.24
	GDC- Ni:Co (1:3)	0.35	4.71
850	GDC	1.30	5.47
	GDC-Co	0.24	1.25
	GDC-Ni	0.25	1.51
	GDC-Cu	0.30	3.58
	GDC- Ni:Co (1:1)	0.32	1.36
	GDC- Ni:Co (3:1)	-	-
	GDC- Ni:Co (1:3)	0.18	1.55

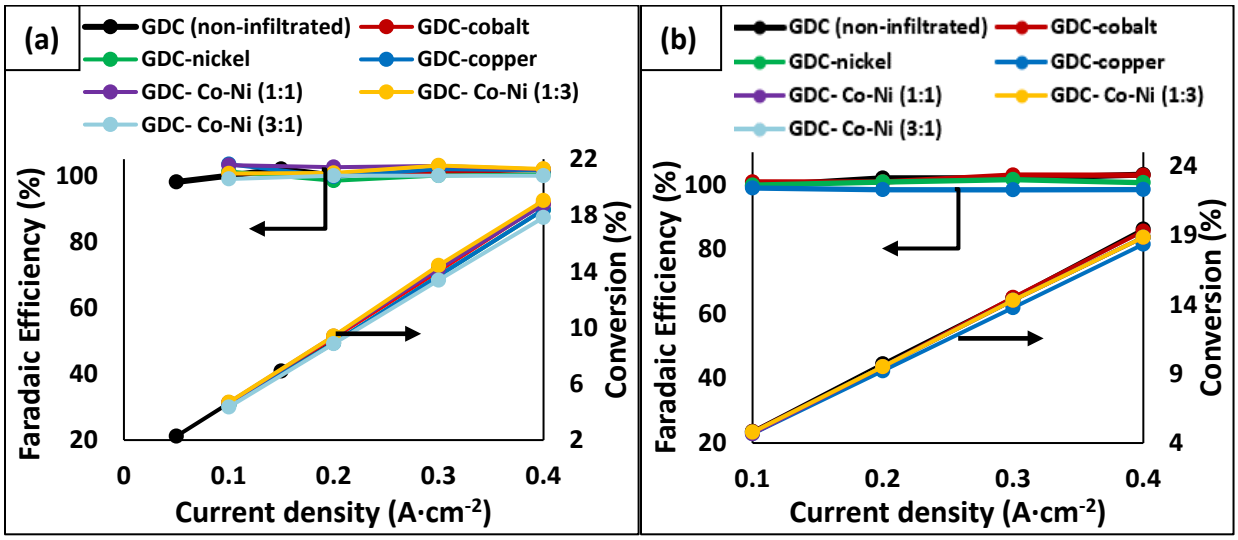

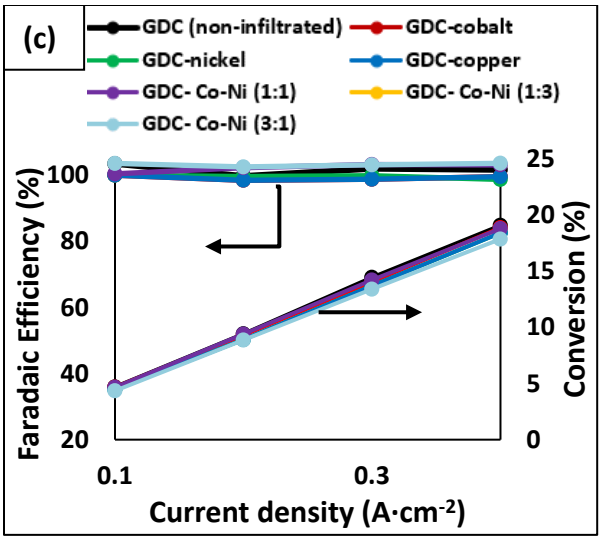

Figure 8. Faradaic efficiency and conversions for cells tested at: a) 750, b) 800, and c) 850 °C.

2.2.4. *Long-term Stability Testing Results*

To determine the stability of the infiltrated solid oxide cells towards CO_2 electroreduction, a cell with Co infiltrated cathode was tested at 850 °C under galvanostatic mode by applying a current density of 0.4 $A \cdot cm^{-2}$ for 48 hours as shown in Figure 9. During the first 24 hours of the testing period, the voltage dropped by 0.1 V thus indicating a slight enhancement in the cell's performance. This enhancement in performance contradicts with the results presented in literature as most solid oxide cells experience performance degradation when tested galvanostatically for long periods of time. Similar results were reported by Green et al. [15] when testing GDC electrodes for 360 hours under different temperatures as well as different $CO:CO_2$ ratios. They related the performance enhancement to the change in the surface morphology of the GDC electrodes over time. During the second 24 hours of the testing period, the voltage was almost constant at a value equal to 1.25 V.

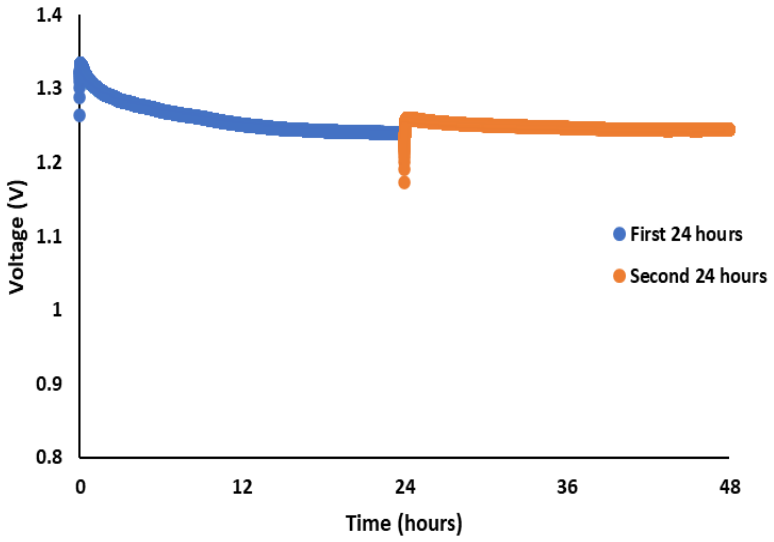

Figure 9. Stability test for cobalt infiltrated cell at 850 °C.

Figure 10 shows the polarization curves and the Nyquist plots collected before and after the stability test. The R_p value was equal to 1.3 $\Omega \cdot cm^2$ while it dropped to 0.98 and 1 $\Omega \cdot cm^2$ after 24 and 48 hours of testing respectively. The low frequency part of the polarization resistance, which represented the mass transfer resistance, was almost constant throughout the testing period with a value equal to 0.6 $\Omega \cdot cm^2$. The drop in the R_p value was due to the drop in the value of the high frequency part of the polarization resistance, which represented the charge transfer resistance.

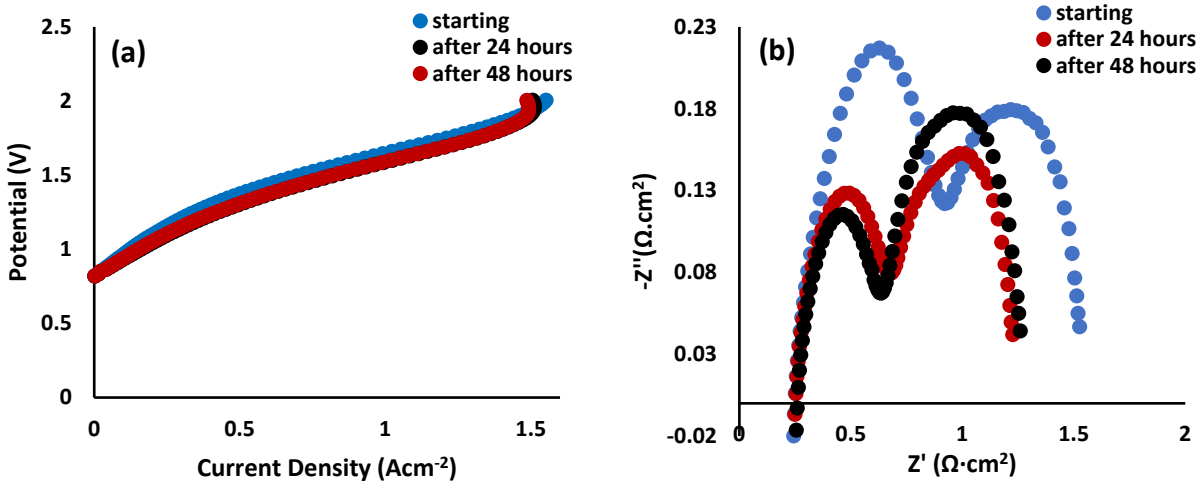

Figure 10. CO_2 electroreduction performance of cobalt infiltrated cell before and after the stability test at 850 °C: (a) Polarization curves and (b) Nyquist curves.

Faradaic efficiency and CO_2 to CO conversion for the cell tested galvanostatically at 850 °C is shown in Figure 11. Throughout the testing period, values for the Faradaic efficiency and conversion were approximately equal to 100% and 19%, respectively. These results were equal to the theoretically calculated values, thus indicating that the Co infiltrated solid oxide cells have good stability towards CO_2 electrochemical reduction.

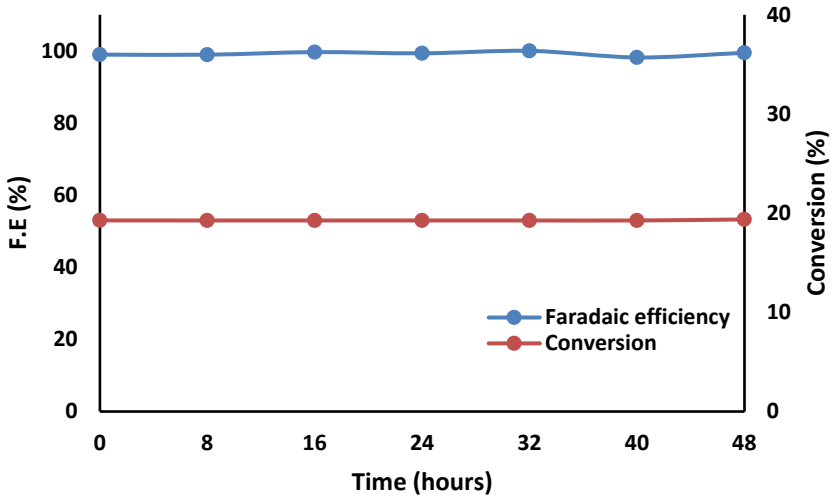

Figure 11. CO_2 Faradaic efficiency and conversion for Co infiltrated cell during galvanostatic test at 850 °C.

2.2.5. *Electrochemical Performance with Simulated Flue Gas*

Two Co infiltrated cells were tested at 800 °C using the gas composition shown in Table 1. To compare the initial electrochemical performance of the tested cells, EIS and polarization curves were obtained after achieving stable OCV values. As shown in Figure 12, both cells showed similar electrochemical performance as the polarization curves and the EIS spectra gave relatively close values. R_s and R_p values for the first cell (Trial_1) were equal to 0.49, and 5.25 $\Omega \cdot cm^2$, respectively, while the R_s and R_p values for the second cell (Trial_2) were equal to 0.38 and 4.85 $\Omega \cdot cm^2$, respectively.

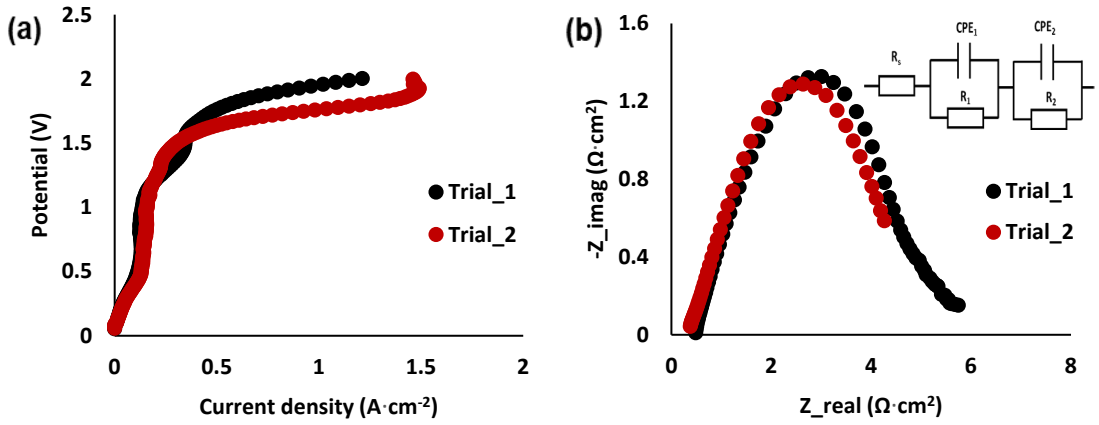

Figure 12. Electroreduction performance of the cells tested at 800 °C using flue gas composition: (a) Polarization curves and (b) Nyquist curves.

Long term galvanostatic testing was then initiated by subjecting the tested cells to a constant current density of 0.4 $A \cdot cm^{-2}$ as shown in Figure 13. In trial_1, the voltage readings were fluctuating constantly between 1.25 and 1.42 V for the first 22 hours of testing, then the voltage values kept increasing slightly for the rest of the testing period. While in trial_2, voltage readings were fluctuating constantly between 1.22 and 1.36 V for the first 12 hours of the testing period, then the voltage fluctuation range increased to be in between 1.38 and 1.54 V. The gas mixture exiting the cathode side of the cell was composed of 60.8 vol.% N_2, 34.6 vol.% CO_2, 2.2 vol.% H_2, and 2.4 vol.% CO during the full testing period of both trials.

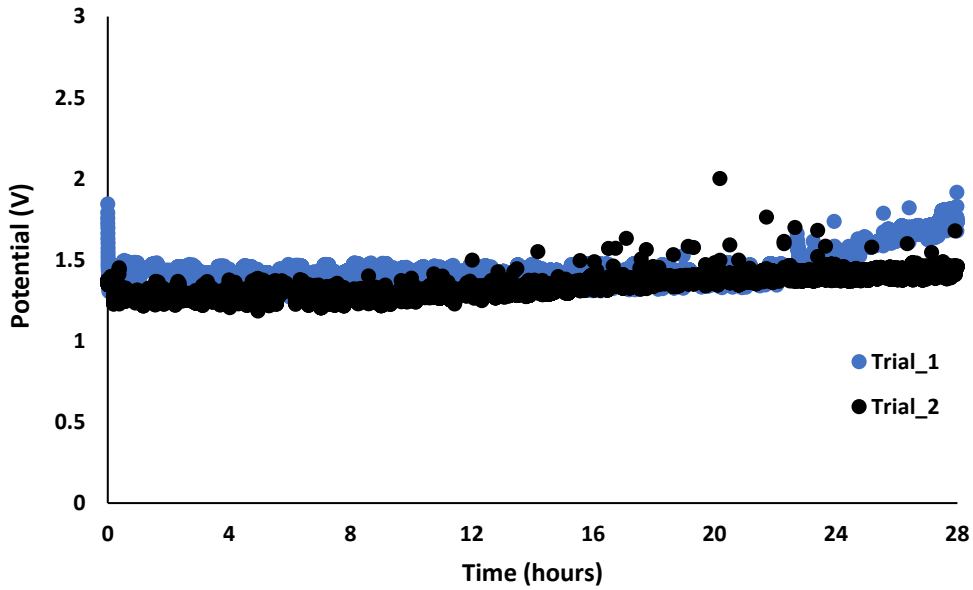

Figure 13. Long term galvanostatic testing for cells under flue gas conditions.

The continuous fluctuation in the voltage readings throughout the galvanostatic test was believed to be occurring due to delamination in one of the current collectors fitted on both sides of the tested cells. Figure 14 shows the current collector after detaching it from the test fixture; delaminated from the cathode side of the cell as can be seen. The delamination is suspected to be occurring due to the presence of O_2 in the gas environment on the cathode side of the cell; this is believed to oxidize the metal electrocatalyst and delaminate it from the silver current collector [16].

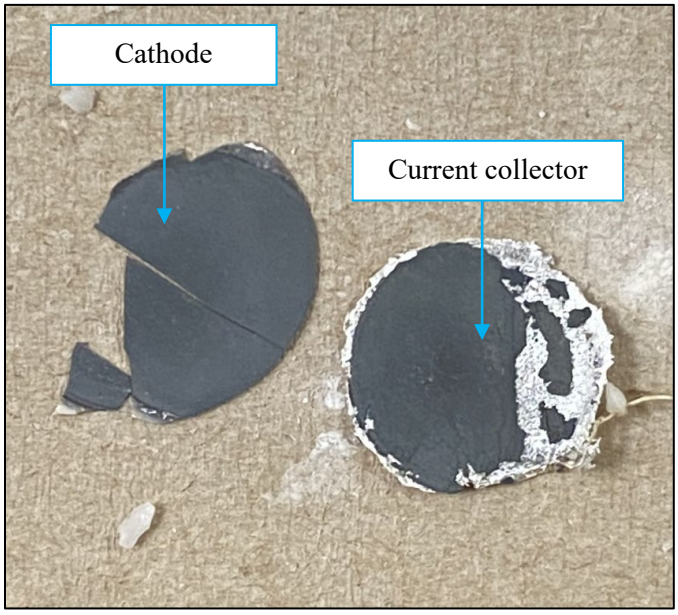

Figure 14. Current collector delaminated from the cathode side of the tested button cell.

2.3. Summary

Transition metal infiltrated cathodes showed marked enhancement in performance towards CO_2 electroreduction in SOECs compared to non-infiltrated cathodes. Also, it was demonstrated in this chapter that the CO_2 electroreduction performance of the tested cells enhanced with increasing operating temperatures due to enhanced reaction kinetics at elevated temperatures. Cells with Co, Ni, And Co-Ni alloy infiltrated cathodes showed almost similar electrochemical performance towards high CO_2 electroreduction which is likely due to their similar oxophilicity. Although, cells with Co infiltrated cathodes deteriorated when tested under flue gas conditions, it survived for 28 hours producing syngas (H_2 and CO).

3. Electrocatalyst Development for Ethane e-ODH Solid Oxide Fuel Cell

To assess the appropriateness of the SOEC platform for conducting the electrochemical-oxidative dehydrogenation (e-ODH) of C_2H_6 to C_2H_4, an SOEC platform featuring an anode active for C_2H_6 oxidation was designed and tested. The general e-ODH SOEC design called for a cathode favorable for reducing atmospheric O_2 to oxygen ions (O^{2-}), an electrolyte for O^{2-} transport, and an anode active for using the O^{2-} to selectively oxidize C_2H_6. Due to its previously recognized applicability for ethane ODH, various compositions of perovskite structured lanthanum-strontium-iron oxide ($La_{1-x}Sr_xFeO_{3-\delta}$ (LSF), where the x of LSFx denotes the x-ratio of lanthanum and strontium in the A-site) electrocatalyst were incorporated into the e-ODH SOEC anode and analytically evaluated [17]. Cells featuring anodes of various LSF compositions were screened for e-ODH performance (evaluated based on C_2H_6 conversion, product selectivity, and C_2H_4 yield) at several different operating temperatures.

3.1. Experimental Methods

3.1.1. *Cell Fabrication*

The e-ODH SOFC design was constructed on 2 cm diameter and 0.15 mm thick ScSZ electrolytes (Fuelcellmaterials, SKU:211214), with the anode and cathode layers constructed on either side. The O_2-reducing cathode was prepared by printing base layers of GDC, interlayers of LSMGDC, and upper layers of LSM20. LSM20 has popularly been used as an electrode material for a variety of applications, including oxygen reduction, warranting its selection for this application [18].

An infiltration approach was used to construct the C_2H_6-oxidizing anode. This approach involved constructing a porous ceramic layer on the anode-side of the electrolyte, known as a scaffold and delivering the metal components of the desired electrocatalyst by a liquid infiltration solution, where the final LSF composition was controlled by the metal component concentrations and additional additives were included to facilitate permeation of the solution throughout the scaffold. The infiltration approach allowed for flexibility in preparing the different LSF compositions within the anode, and the prior sintering of the porous layer allowed for reliable sintering of the ceramic components without risking a solid-state reaction with the metal electrocatalyst components [19–21].

The porous scaffold was constructed by mixing YSZ powder sieved at 120 mesh (125 μm), poly(methyl)methacrylate (PMMA) microspheres (5-20 μm), and a terpineol-based ink vehicle. To reduce moisture content, the YSZ powder and PMMA microspheres were stored in a 110 °C oven. Ink mixtures were prepared containing 40 wt.% ink vehicle and 60 wt.% solids, with the solids being composed of 80 wt.% YSZ and 20 wt.% PMMA. This ink was screen printed onto the anode side of the electrolyte, and then the cells were sintered to drive off the organic components (the ink vehicle and PMMA) and fuse the YSZ powder particles into the porous layer.

The resulting LSF composition was determined by the concentrations of metal in the infiltration solution. Metals were introduced into solution by preparing stock solutions of dissolved metal nitrates of the LSF components, then using aliquots of the metal nitrate stock solutions to prepare the infiltration solution. Work to identify acceptable LSF infiltration solution compositions began with infiltrating to form LSF1.00, with the expectation that producing a perovskite structured material would be easiest with a single element composing the A-site (strontium, in the case of LSF1.00). The precursor metal concentrations in the LSF1.00 infiltration solution were 0.50 M strontium and 0.50 M iron, reflecting the 1:1 molar ratio of Sr to Fe in the desired phase. Additional components in the infiltration solution were

used to promote the dissolution of the metal species and to facilitate contact between the solution and the scaffold [19–21]. Of the chelating agents and compositions tested when preparing the LSF1.00 solution, it was found that a composition of 0.125 M citric acid resulted in good metal distribution by SEM/EDS analysis and good LSF1.00 phase detection by XRD analysis [20]. As a surfactant, 0.2 g of Triton-X100 was added to the 25 mL volumetric flask in which the solution was prepared [20]. To improve wetting, the solution was diluted with ethanol [21]. Once the infiltration solution was delivered, the cells were calcined at 900 °C for six hours for all LSF compositions.

The LSF electrocatalyst produced by infiltration with an LSF precursor solution was evaluated using SEM, EDS, and XRD. SEM/EDS provided information regarding the distribution of the metals throughout the scaffold and permeation of the metals into the scaffold. XRD analysis would indicate the strength of response for perovskite-specific peaks relative to single metal oxide or solid-phase reaction product peaks.

LSF1.00 infiltration solution development indicated that having a total metal weight concentration around 72 g/L produced acceptable metal loadings while allowing permeation of the metal to where the scaffold met the bulk electrolyte. This metal weight concentration was used as a target for defining the metal concentrations of the infiltration solutions for the other LSF compositions, namely LSF0.00, LSF0.25, LSF0.50, and LSF0.75. The overall metal and chelating agent compositions used to prepare the tested LSF electrocatalysts are tabulated in Table 3.

Table 3. Metal and chelating agent concentrations used for the infiltration solutions to prepare various LSF compositions.

LSF composition	La molarity	Sr molarity	Fe molarity	Chelating agent / molarity
LSF0.00	0.37 M	N/A	0.37 M	Citric acid/0.125 M
LSF0.25	0.30 M	0.10 M	0.39 M	Glycine/0.25 M
LSF0.50	0.21 M	0.21 M	0.42 M	Glycine/0.25 M
LSF0.75	0.11 M	0.34 M	0.46 M	Citric acid/0.125 M
LSF1.00	N/A	0.50 M	0.50 M	Citric acid/0.125 M

3.1.2. *e-ODH Testing Setup*

The e-ODH testing setup required the control of the gas environments at the anode and cathode sides of the cell, the control of the cell's operating temperature, the means of electrochemically running the cell, and the capacity to analyze the gas-species products in the cell's product gas stream. Tests were conducted on e-ODH SOFCs featuring anodes containing LSF0.00, LSF0.25, LSF0.50, LSF0.75, and LSF1.00, with operating temperatures of 700, 725, and 750 °C. Two cells were run for each combination of LSF composition and operating temperature, so that the original and duplicate data sets could be compared for reproducibility in cell performance.

During testing, the cells were mounted on a fixture to control the gas environments at the anode and cathode sides of the cell. The oxygen-reducing cathode faced outwards to the air, where an airline flowing 200 sccm of air circulated fresh air across the cathode. The C_2H_6-oxidizing anode faced inwards towards an internal flow path, where a fuel mixture of 96 vol.% C_2H_6 and 4 vol.% N_2 was delivered across the

anode at 80 sccm. An Aremco 617 glass-ceramic sealant was used to hold the cell to the fixture and to isolate the air environment of the cathode from the fuel environment of the anode.

The fixture contained an internal heating coil and was housed in a tube furnace. Because the fixture only extended into the tube furnace a short distance, the furnace provided general temperature control while the heating coil provided precise temperature control to maintain the operational temperature. The cell was electrochemically operated with a Gamry potentiostat using a four-probe configuration, with applied current densities of 0.00, 0.10, 0.20, 0.25, 0.30, 0.40, and 0.50 $A \cdot cm^{-2}$.

Gas species analysis of the product stream was conducted using a GC that was connected to the outlet flow path of the cell. Product stream concentrations of H_2, O_2, N_2, CH_4, CO, CO_2, C_2H_4, and C_2H_6 could be quantified by the GC. The quantified GC data for the gas species components could be used.

3.2. Results

3.2.1. *Characterization of Fabricated Cells*

The cross-sectional SEM image in Figure 15 illustrates the porous scaffold produced by printing with a solids content of 80 wt.% YSZ and 20 wt.% PMMA.

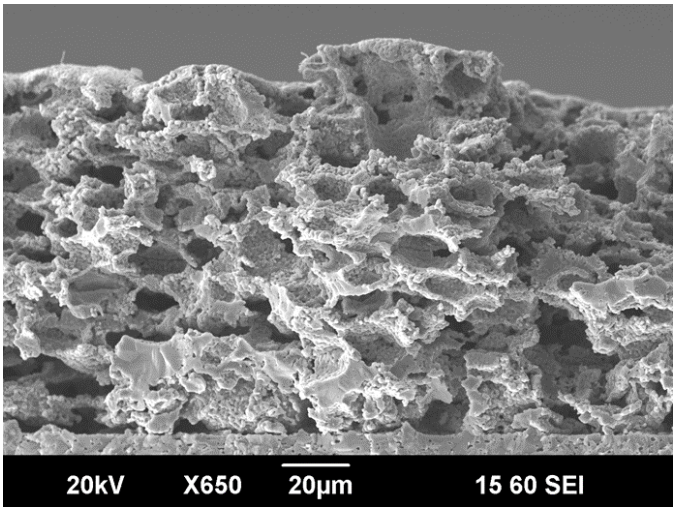

Figure 15. Cross-sectional SEM image of a porous YSZ layer produced by screen printing with an ink solids content of 80 wt.% YSZ powder and 20 wt.% PMMA microspheres.

SEM cross-sectional images indicated scaffolds 100±20 µm thick, with pores 20-40 µm. Figure 16 shows SEM/EDS cross-sectional images for the resulting LSF1.00 deposition in the infiltrated cell, and Figure 17 shows the XRD analysis of the surface of the LSF1.00 infiltrated anode.

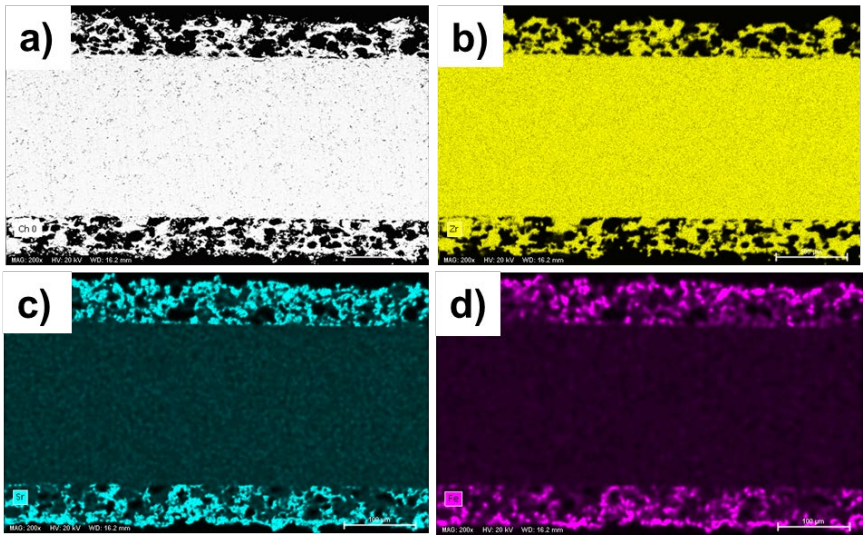

Figure 16. SEM /EDS cross-sectional images of cells infiltrated with the LSF1.00 precursor solution, showing a) the starting backscatter image, b) zirconia content, c) strontium content, and d) iron content. The cell cross-section images show the bulk electrolyte with porous YSZ layers on the top and bottom, with both layers having been infiltrated for LSF1.00.

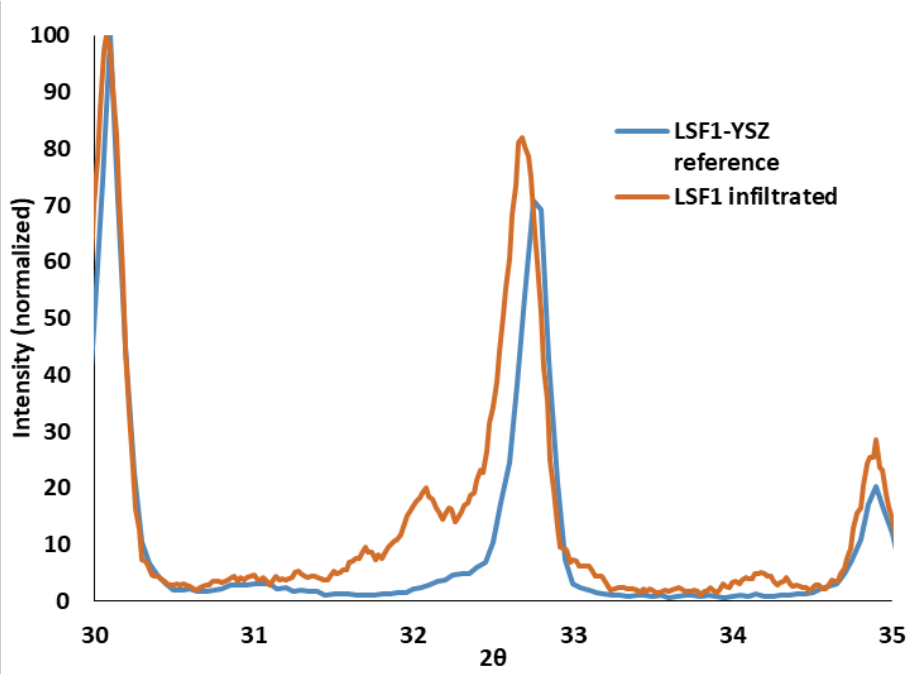

Figure 17. XRD scan comparing the infiltrated LSF1.00 anode response around a perovskite-specific peak to a reference mixture of LSF1.00 and YSZ powders.

The SEM/EDS and XRD analyses described above were used to evaluate the effect that different chelating agents and concentrations had on the resulting electrocatalysts of the other LSF compositions, which was necessary to account for any issues with A-site lanthanum-strontium substitution for the intermediate LSF compositions.

3.2.2. *Electrocatalyst Screening Results*

Data sets were collected for original and duplicate e-ODH SOECs featuring anodes of LSF0.00, LSF0.25, LSF0.50, LSF0.75, and LSF1.00 and operated at 700, 725, and 750 °C. The C_2H_6 conversion, C_2H_4 yield, and product selectivities for the various LSF compositions tested at 700 °C at increasing applied current densities are shown in Figure 18, where the error bars reflect the standard deviation between the original and duplicate data sets. Analogous data for testing at 725 °C is shown in Figure 19 and for 750 °C in Figure 20.

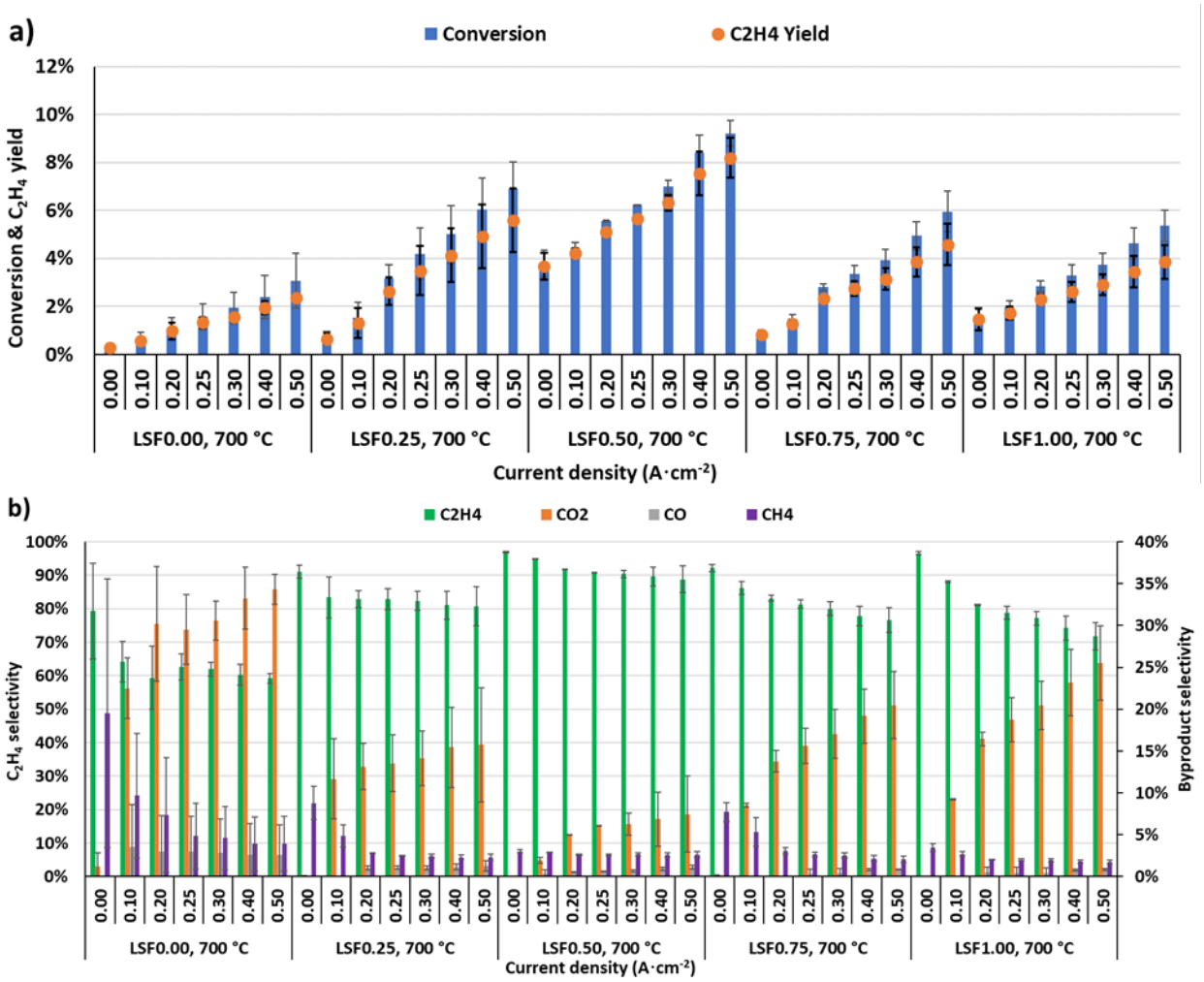

Figure 18. Operational e-ODH SOEC results for operation at 700 °C, showing a) C_2H_6 conversion and C_2H_4 yield, and b) product selectivity.

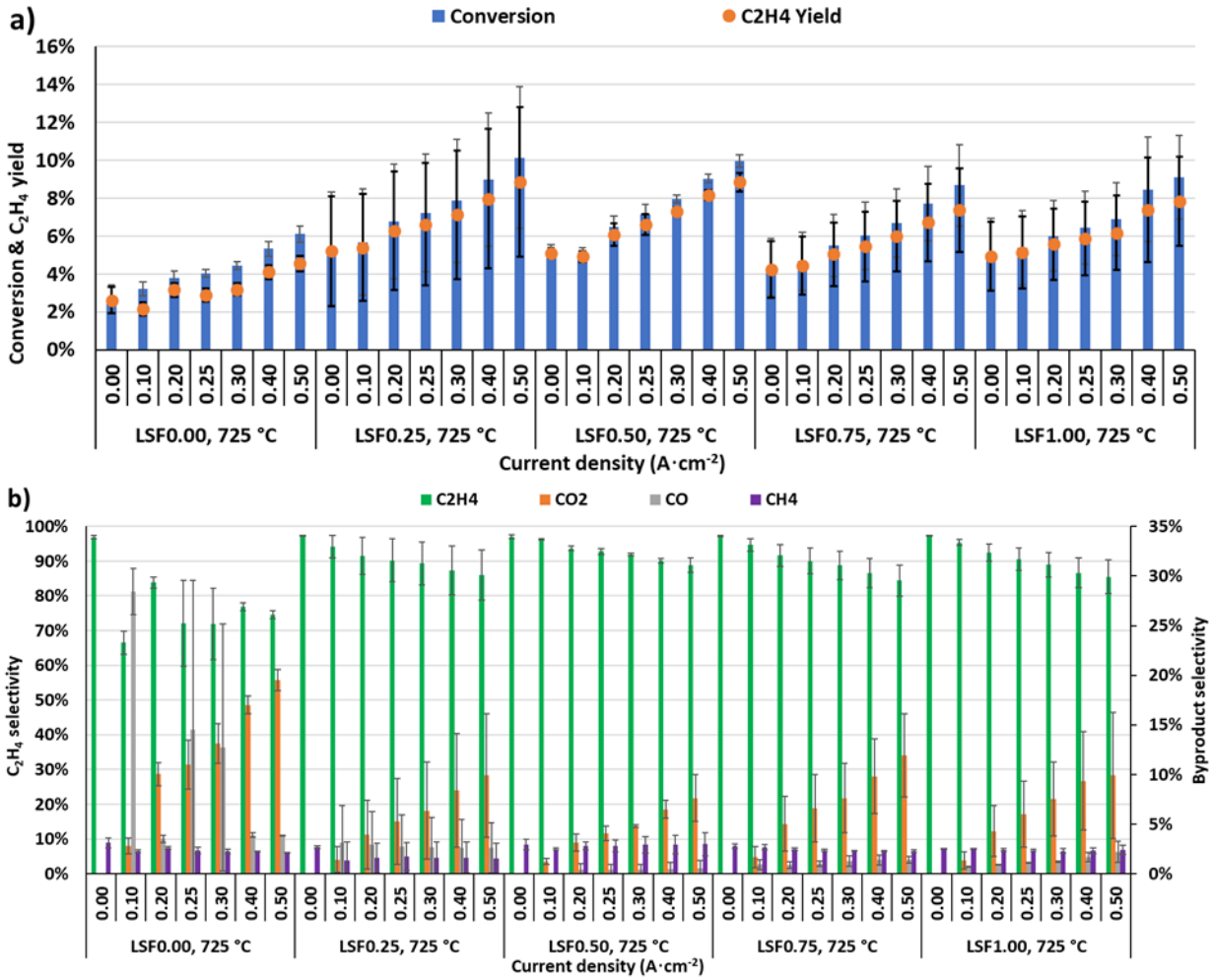

Figure 19. Operational e-ODH SOEC results for operation at 725 °C, showing a) C_2H_6 conversion and C_2H_4 yield, and b) product selectivity.

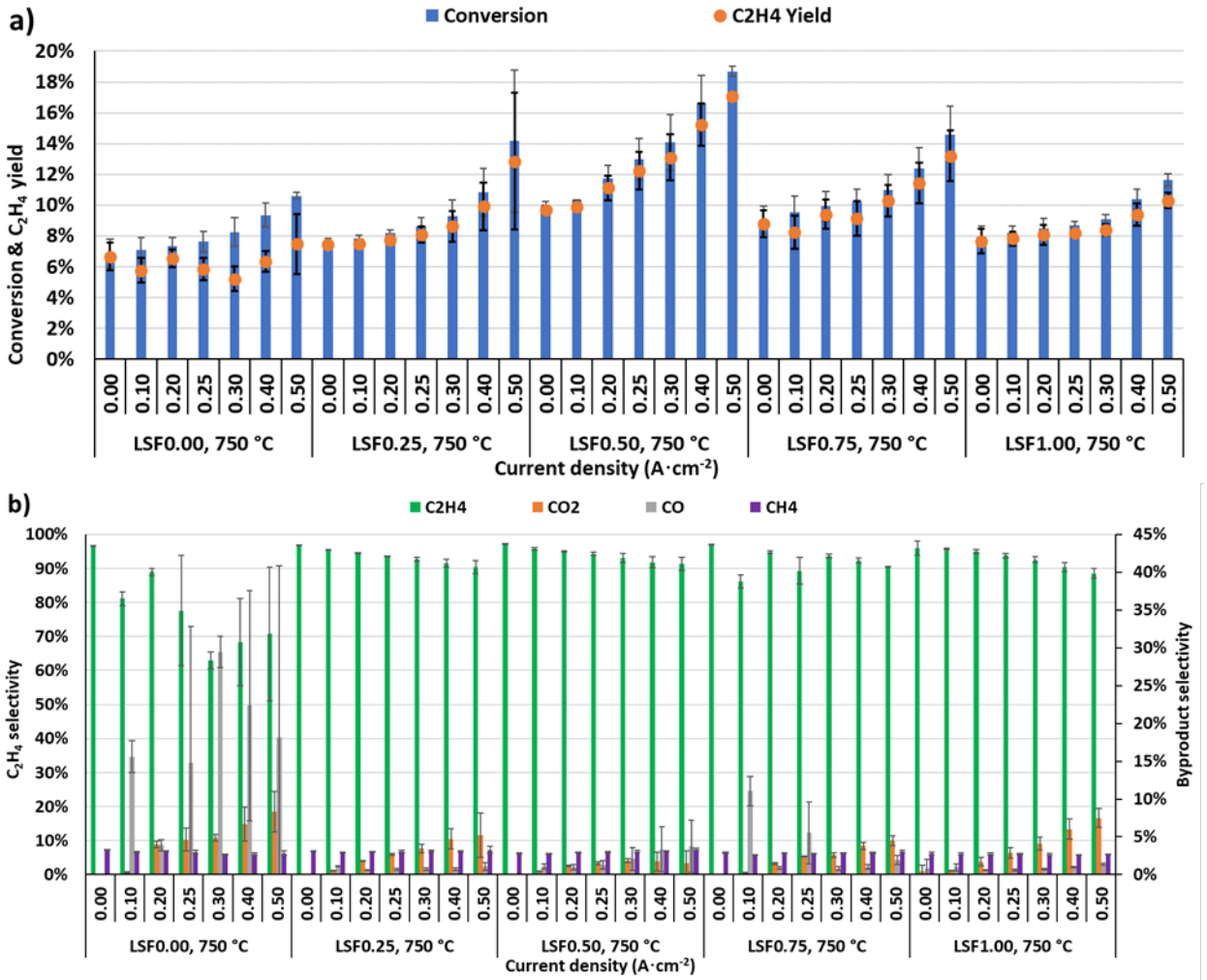

Figure 20. Operational e-ODH SOEC results for operation at 750 °C, showing a) C_2H_6 conversion and C_2H_4 yield, and b) product selectivity.

Several trends were readily apparent for the various tested LSF compositions. Generally, as the operating temperature of the cell increased, C_2H_6 conversion and C_2H_4 selectivity would increase as well. As the applied current density was increased, C_2H_6 conversion would increase while C_2H_4 selectivity would decrease. Of the different LSF compositions, LSF0.50 displayed notably high and consistent performance, a trend that appeared at each operating temperature. When running at 750 °C with 0.5 $A \cdot cm^{-2}$ applied current density, C_2H_6 e-ODH over LSF0.50 averaged an C_2H_6 conversion of 19% with an C_2H_4 selectivity of 91%, for an C_2H_4 yield of 17%.

Based on GC quantification of the carbon-containing gas species, carbon deposition onto the anode could be estimated as the difference between the estimated amount of carbon fed (based on the carbon-nitrogen fuel ratio and the nitrogen measured by the GC during the cell run) and the amount of carbon in the gas species [22]. This estimation was expressed as a percentage of estimated carbon deposited relative to the estimated carbon fed. Estimated carbon deposition percentages are displayed in Figure 21 for the various

LSF composition and operating temperature combinations, with error bars reflecting the standard deviation between the original and duplicate data sets for each combination.

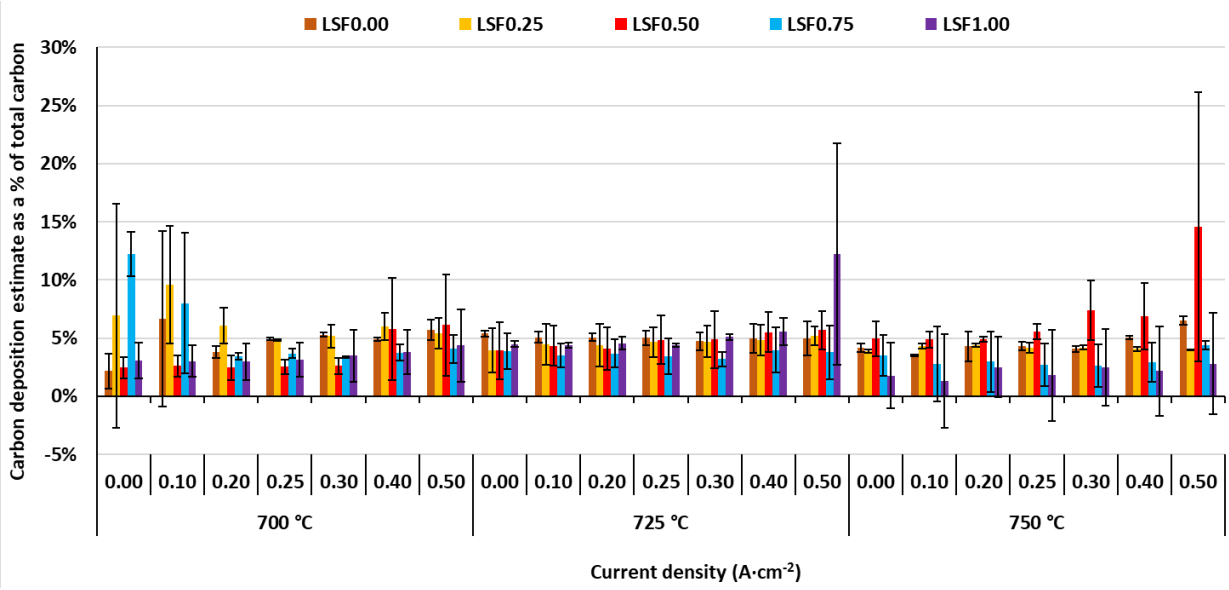

Figure 21. Estimated carbon deposition on the e-ODH anode expressed as a percentage of the estimated total carbon fed.

Based on the estimations, carbon deposition fluctuated around 5% of the fed carbon without showing clear trends relative to changes in operating temperature, LSF composition, or applied current density. In a few instances, the carbon deposition estimations produced negative values for the percentage of carbon deposited. This possibly could have arisen from previously deposited carbon being later reacted into a gas phase species.

3.3. Summary

The fabrication of e-ODH SOFCs and screening tests of different anode LSF electrocatalysts has demonstrated the applicability of the SOFC design for highly selective oxidative dehydrogenation of C_2H_6 to C_2H_4 over LSF electrocatalysts. Of the tested LSF compositions at the various operating temperatures, LSF0.50 demonstrated favorable and consistent C_2H_6 conversion and C_2H_4 selectivity, with C_2H_6 e-ODH over LSF0.50 averaging 19% C_2H_6 conversion, 91% C_2H_4 selectivity, and 17% C_2H_4 yield when operated at 750°C with 0.5 $A \cdot cm^{-2}$ applied current density. Estimation of carbon deposition demonstrated no particular trends with respect to changes in LSF composition, operating temperature, and applied current density.

4. CO_2/e-ODH

In this chapter, the performance of in-house made button SOECs was evaluated for simultaneous CO_2 reduction at the cathode and C_2H_6 oxidation at the anode.

4.1. Experimental Methodologies

4.1.1. *Cell Fabrication*

Researching the feasibility of the joint operation of a CO_2 electrolysis cathode and an ethane e-ODH anode began with developing a single cell featuring the respective cathode and anode, based on the experience gained from the earlier portions of the project. The joint CO_2 reduction cathode/ C_2H_6 e-ODH anode cell design was built on an ScSZ electrolyte, with both electrodes fabricated using infiltration approaches adapted from the cell preparations described in the previous sections. For the C_2H_6 e-ODH anode, a porous YSZ scaffold was prepared by screen printing an ink mixture with a solids content of 80 wt.% YSZ powder and 20 wt.% PMMA microspheres (5-20 μm), followed by sintering at 1500 °C for four hours. When fabricating the cathode, two GDC10 base layers were initially screen printed on the scaffold and were then sintered at 1300 °C for 10 hours. After sintering the GDC10 interlayers, six layers of the cathode powder (20 wt.% coke powder-80 wt.% GDC10) were screen printed on top of it and were then sintered at 1300 °C for 10 hours to create a porous cathode structure. A cross-sectional diagram of the electrolyte and electrode scaffold layers is shown in Figure 22.

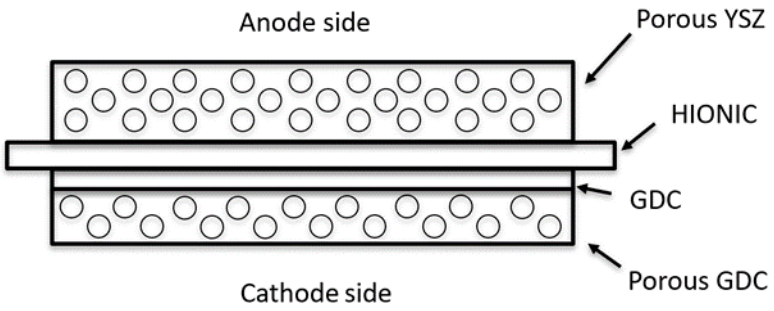

Figure 22. Cross-sectional diagram of joint CO_2 reduction cathode/ethane e-ODH anode cell.

C_2H_6 e-ODH anode electrocatalyst was prepared by infiltrating the porous YSZ scaffold with the solution described in the previous section to prepare LSF1.00 while the CO_2 electrolysis cathode was prepared by infiltrating the porous GDC scaffold with Co transition metal electrocatalyst. The fabricated cells were calcined at 900 °C for 6 hours.

4.2. Materials Characterization

The anode and cathode sides of the infiltrated cells were examined by XRD to identify the metal oxide phases present after calcination.

4.3. Electrochemical Testing Setup

Silver current collectors were attached to both sides of the fabricated cell using a conducting silver paint. The cell was then secured to an e-ODH alumina tube and a regular alumina tube with the anode side facing the inside of the e-ODH tube and the cathode side facing the inside of the regular one. The two alumina tubes were attached together by applying two layers of a water-based glass sealant (Aremco, item no: 617), two layers of a water-based fast curing alumina sealant (Cotronics, item no: 989FS-1), and two layers of a ceramic-glass sealant (Mosci, item no: GL1862), respectively. The assembled fixture was then placed inside a small tube furnace (DS-Fibertech, item no: TS06002) as shown in Figure 23.

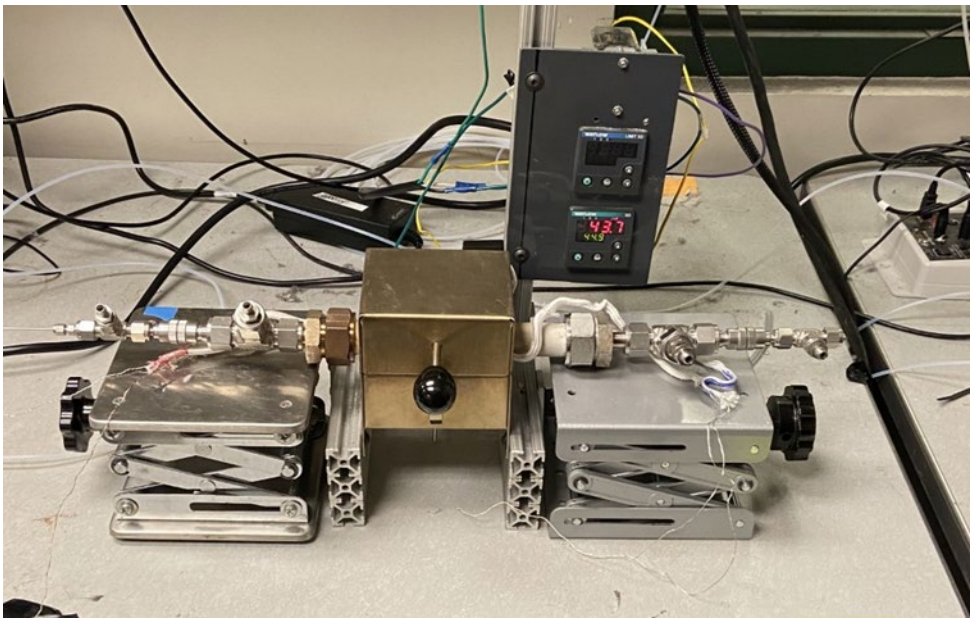

Figure 23. e-ODH gas delivery fixture (left) and CO_2 gas delivery fixture (right) positioned within the small tube furnace.

Before the electrochemical testing was initiated, pure Ar was flown on both sides of the cell and was analyzed by a GC to verify that both sides of the cell were sealed to the atmosphere and that cross flow was not occurring between one side to the other. Once leak checking was complete, both sides of the cell were reduced by flowing 80 sccm of 10 vol.% H_2/Ar for one hour. After reduction, 80 sccm of 96 vol.% C_2H_6/N_2 was supplied to the anode side while 50 sccm of a blend composed of 10 vol.% CO, 81 vol.% CO_2, and 9 vol.% N_2 was supplied to the cathode side, and testing could begin, by applying different current densities (0.0, 0.1, 0.2, 0.3, 0.4, and 0.5 $A \cdot cm^{-2}$) using a potentiostat. The produced gases from both sides of the cell were analyzed using two separate GC analyzers.

4.3.1. *Characterization of Fabricated Cells*

Both sides of the fabricated CO_2/e-ODH cell were analyzed using XRD to confirm that LSF1.0 perovskite phase was formed on the anode side and Co_3O_4 was formed on the cathode side. From Figure 24, it can be seen that the desired catalyst phases are formed on the electrodes of the fabricated cells.

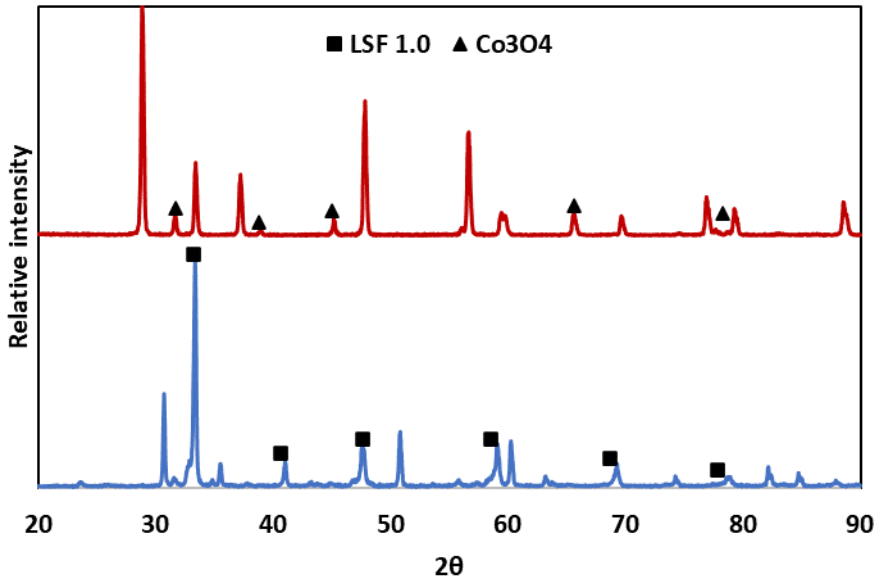

Figure 24. XRD patterns for the electrodes of CO_2/e-ODH cell.

4.3.2. *Electrochemical Testing Results*

Figure 25 shows the polarization curves and the Nyquist plots for two CO_2/e-ODH cells tested at 725 °C. Both cells showed different performance, thus suggesting a possible variation in one of the experimental parameters between both replicates. It was believed that temperature was most likely to be varied between both runs due to the different OCP, and R_s values.

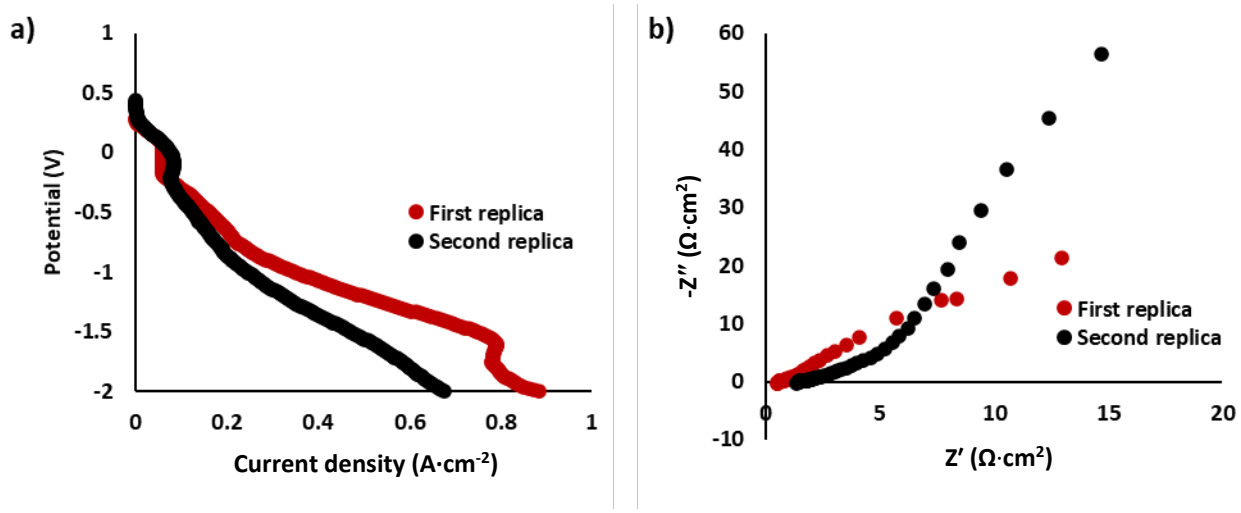

Figure 25. Electrochemical performance of the CO_2/e-ODH cells at 725 °C: a) Polarization curves; b) Nyquist plots.

The CO_2 to CO conversions and faradaic efficiency for both replicates are shown in Figure 26. The CO_2 conversion increased linearly with increasing currents but dropped significantly at 0.5 A·cm^{-2}. Similarly, CO_2 Faradaic efficiency was above 95% for all current densities except for 0.5 A·cm^{-2} where it dropped

below 95% and was equal to 89%. The drop in the faradaic efficiency and conversion values might be due to cell degradation as a results of coke formation on the anode side. Moreover, the degradation might also be due to the temperature imbalance that was noticed on both sides of the cell.

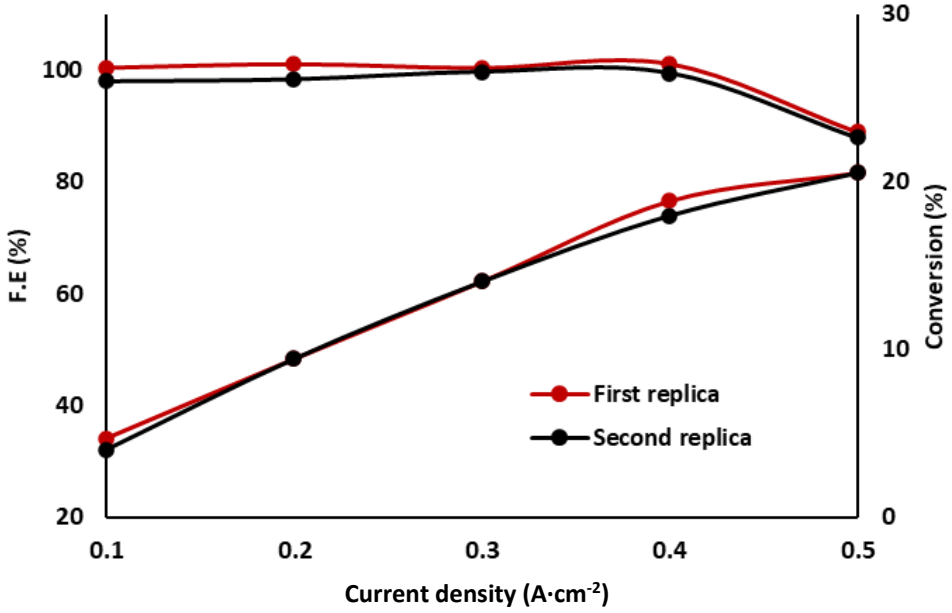

Figure 26. CO_2 reduction performance as characterized by Faradaic efficiency (F.E) and CO_2 conversion.

Regarding C_2H_6 e-ODH anode performance, Figure 27 shows the averaged C_2H_6 conversion, C_2H_4 yield, and product selectivity for the two runs, with the error bars representing the standard deviation between the two runs.

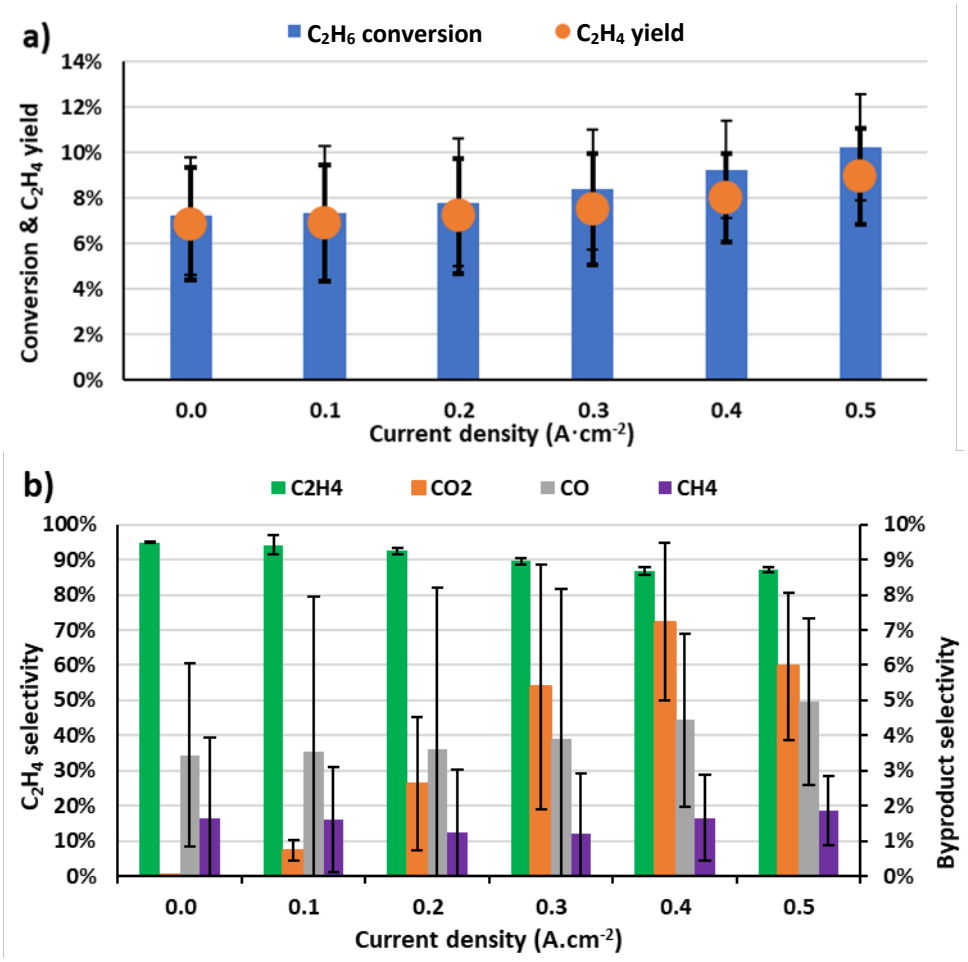

Figure 27. Ethane e-ODH performance of the joint cell, characterized by averaged a) ethane conversion and ethylene yield, and b) product selectivities.

Based on the product selectivity averages, both runs displayed C_2H_4 selectivity in the 80% to 90% range. Between the two runs, C_2H_6 conversion and subsequently C_2H_4 yield showed variability, relative to the trends toward consistency observed during the earlier LSF electrocatalyst e-ODH screening tests. C_2H_6 conversion differences, similar to the electrochemical characterization comparison differences described above, could have arisen from challenges in managing the joint cell's operating temperature.

4.4. Summary

This chapter demonstrated the viability of performing simultaneous CO_2 reduction and C_2H_6 oxidation in SOECs. Analysis of the ethane e-ODH anode performance showed consistent and high ethylene production between the original and duplicate cell runs, although greater difference was seen in the C_2H_6 conversion and ethylene yield values observed between the two runs.

5. Lifecycle and Techno-economic Analyses

This chapter presents preliminary LCA and TEA results for an SOEC CO_2 utilization process producing CO from biogas.

5.1. Methodologies

5.1.1. *Model Assumptions*

A zero-order dimensional steady state isothermal model was used to simulate the system. Biogas was utilized as the source of CH_4 and CO_2 for the process. All working fluids were assumed as ideal gas with no pressure drop. An existing solid oxide fuel cell (SOFC) model was modified to account for SOEC operation. Details of the previous model may be found in literature [23,24].

5.1.2. *Process Flow Model*

The schematic of the SOEC process is shown in Figure 28. The heated biogas was compressed and mixed with the recirculated anode exhaust. The split fraction of the splitter module was adjusted to maintain a desired H_2O/C ratio of 0.5 at the reformer inlet. The incoming air flow rate to the reformer was controlled by using a design specification block of Aspen Plus to make the reformer adiabatic in order to achieve maximum reforming efficiency without any external heat addition. At steady state, the reformer outlet stream primarily contains H_2 and CO with a small percentage of CH_4.

A Gibbs reactor was used to model the anode half-cell reaction, while a stoichiometric reactor was used to simulate the electroreduction of CO_2 to CO and a separator to transport O_2 to the anode. Unreacted fuel was burned with air in a post-combustor. A heat exchanger was used to recover thermal energy generated via the post-combustor and Joule heating in the SOEC. A separator was used to mimic a CO_2 membrane to generate the CO product.

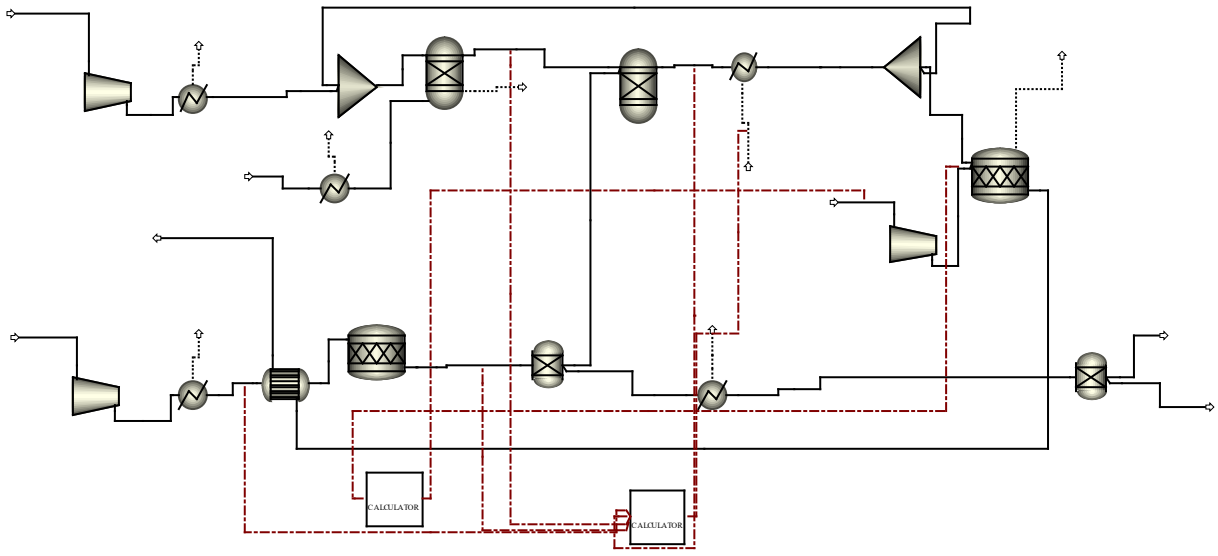

Figure 28. SOEC process simulation schematic.

5.2. Lifecycle Analysis

The SOEC process was designed to generate 500 kscf/day CO. In comparison, commercial CO production systems generate 50 kscf/day to over 10 million scf/day. The SOEC process was assumed to operate on electrical power only. Thermal energy generated by the SOEC stacks (Joule heating), and anode exhaust post-combustor were thermally integrated into the system. Material and energy balances for the process are summarized in Table 4.

Table 4. SOEC process material and energy balances.

Parameter	Value
CO_2 Conversion	25.48 tonnes/day
CO Production	16.21 tonnes/day
Biogas Conversion	138 kscf/day
CO_2 Emissions	7.1 tonnes/day
Power Consumption	124.3 MWh

The LCA study was conducted to compare CO_2 emissions associated with CO production via steam methane reforming (SMR) to the SOEC process. Estimates for SMR CO_2 footprint range from 0.97-1.63 $kgCO_2/kgCO$. At current U.S. electrical power CO_2 emissions rate of 386 $kgCO_2/MWh$ delivered [25], the estimated SOEC CO_2 footprint is 1.8 $kgCO_2/kgCO$. To achieve 0.48 $kgCO_2/kgCO$ (50% reduction of SMR CO_2 footprint) electrical power with a CO_2 emissions rate of 211 $kgCO_2/MWh$.

5.3. Techno-economic Analysis

Results from the process simulation described in Section 5.2 were used to develop a techno-economic analysis for generating CO from CO_2 utilizing the SOEC technology. SOFC stack [26] and balance of plant capital cost [27] values were derived from U.S. DOE sponsored studies and updated to 2021 dollars. Capital and operating costs for CO_2 separation membrane systems were obtained from recently published peer-reviewed literature [28]. No land costs were incorporated into the capital expenditures as the location producing biogas was assumed to possess sufficient room for the SOEC plant. Cost parameters used in the baseline CO required sales price in 2021 dollars per thousand standard cubic feet ($/kscf) included SOFC stack cost ($2,260/stack), natural gas ($6/MMBtu), and electricity ($122/MWh).

Table 5 presents results from the baseline TEA (±30%), estimating a CO required sales price (RSP) of $39.27/kscf. Sensitivity analyses were also conducted evaluating the influence of SOEC stack cost ($1,330-3,200/stack), biogas ($4-8/kscf), and electricity ($75-160/MWh). Results from the sensitivity analyses indicated SOEC stack and biogas had limited impact on CO RSP, resulting in price differentials of ±1.6% for each parameter. Electricity pricing had significant impact on CO RSP, resulting in price differentials ranging from $26.60-$49.95/kscf.

Table 5. SOEC Baseline TEA Study Results (2021 dollars).

Parameter	**Value**
CO Production (mscf/day)	500
Capacity Factor	0.90
Levelized Capital Charge Factor	0.118
Capital Expenses	**Value ($M)**
SOEC	$955
SOEC Balance of Plant	$1,236
Membranes	$304
Total Installed Capital	$2,496
Operating Expenses	**($/kscf)**
Cost of Capital	$1.82
Biogas	$1.87
Electricity	$34.28
Membrane Operation	$1.30
CO RSP Cost	$39.27

5.4. Summary

The preliminary LCA study indicates the proposed SOEC process has potential to manufacture CO with a lower embodied CO_2 emissions than the SMR process. For this to occur, the SOEC technology is coupled with low-carbon intensity electrical power, ideally a renewable energy source, and utilizes CH_4 and CO_2-derived from non-fossil sources such as biogas or landfill gas. The TEA indicates a possible CO RSP range of $26.60/kscf - $49.95/kscf, with the RSP being highly sensitive to the price of electricity. In comparison to current CO sales pricing, the SOEC process may have potential for use in low-volume applications.

References

[1] 2015, *Ullmann's Energy: Resources, Processes, Products*.

[2] 2018, "HyCO Praxair Interview."

[3] Gunardson, H., 1998, *Industrial Gases in Petrochemical Facilities*, Marcel Dekker, Inc.

[4] Graves, C., Ebbesen, S. D., and Mogensen, M., 2011, "Co-Electrolysis of CO_2 and H_2O in Solid Oxide Cells: Performance and Durability," Solid State Ionics, 192(1), pp. 398–403.

[5] Xie, Y., Xiao, J., Liu, D., Liu, J., and Yang, C., 2015, "Electrolysis of Carbon Dioxide in a Solid Oxide Electrolyzer with Silver-Gadolinium-Doped Ceria Cathode," J. Electrochem. Soc., 162(4), p. F397.

[6] Gu, X.-K., Carneiro, J. S. A., and Nikolla, E., 2017, "First-Principles Study of High Temperature CO_2 Electrolysis on Transition Metal Electrocatalysts," Ind. Eng. Chem. Res., 56(21), pp. 6155–6163.

[7] Song, J.-H., Jung, M. G., Park, H. W., and Lim, H.-T., 2013, "The Effect of Fabrication Conditions for GDC Buffer Layer on Electrochemical Performance of Solid Oxide Fuel Cells," Nano-Micro Lett., 5(3), pp. 151–158.

[8] Khan, M. Z., Song, R.-H., Lee, S.-B., Lee, J.-W., Lim, T.-H., and Park, S.-J., 2014, "Effect of GDC Interlayer on the Degradation of Solid Oxide Fuel Cell Cathode during Accelerated Current Load Cycling," International Journal of Hydrogen Energy, 39(35), pp. 20799–20805.

[9] Kuboon, S., and Hu, Y. H., 2011, "Study of NiO−CoO and Co_3O_4−Ni_3O_4 Solid Solutions in Multiphase Ni−Co−O Systems," Ind. Eng. Chem. Res., 50(4), pp. 2015–2020.

[10] Tian, Y., Zhang, L., Jia, L., Wang, X., Yang, J., Chi, B., Pu, J., and Li, J., 2019, "Novel Quasi-Symmetrical Solid Oxide Electrolysis Cells with in-Situ Exsolved Cathode for CO_2 Electrolysis," Journal of CO2 Utilization, 31, pp. 43–50.

[11] Riegraf, M., Amaya-Dueñas, D. M., Sata, N., Friedrich, K. A., and Costa, R., 2021, "Performance and Limitations of Nickel-Doped Chromite Anodes in Electrolyte-Supported Solid Oxide Fuel Cells," ChemSusChem, 14(11), pp. 2401–2413.

[12] Yue, X., and Irvine, J. T. S., 2012, "Alternative Cathode Material for CO_2 Reduction by High Temperature Solid Oxide Electrolysis Cells," J. Electrochem. Soc., 159(8), p. F442.

[13] Kaur, G., Kulkarni, A. P., Giddey, S., and Badwal, S. P. S., 2018, "Ceramic Composite Cathodes for CO_2 Conversion to CO in Solid Oxide Electrolysis Cells," Applied Energy, 221, pp. 131–138.

[14] Li, Y., Xie, K., Chen, S., Li, H., Zhang, Y., and Wu, Y., 2015, "Efficient Carbon Dioxide Electrolysis Based on Perovskite Cathode Enhanced with Nickel Nanocatalyst," Electrochimica Acta, 153, pp. 325–333.

[15] Green, R. D., Liu, C.-C., and Adler, S. B., 2008, "Carbon Dioxide Reduction on Gadolinia-Doped Ceria Cathodes," Solid State Ionics, 179(17), pp. 647–660.

[16] Pan, Z., Liu, Q., Yan, Z., Jiao, Z., Bi, L., Chan, S. H., and Zhong, Z., 2022, “On the Delamination of Air Electrodes of Solid Oxide Electrolysis Cells: A Mini-Review,” Electrochemistry Communications, 137, p. 107267.

[17] Yi, G., Hayakawa, T., Andersen, A. G., Suzuki, K., Hamakawa, S., York, A. P. E., Shimizu, M., and Takehira, K., 1996, “Oxidative Dehydrogenation of Ethane over $La_{1-x}Sr_xFeO_{3-\delta}$ Perovskite Oxides,” Catalysis Letters, 38(3), pp. 189–195.

[18] Sikalidis, C., ed., 2011, *Advances in Ceramics: Synthesis and Characterization, Processing and Specific Applications*, BoD – Books on Demand. ISBN 978-953-307-505-1.

[19] Cheng, Y., Yu, A. S., Li, X., Oh, T.-S., Vohs, J. M., and Gorte, R. J., 2015, “Preparation of SOFC Cathodes by Infiltration into LSF-YSZ Composite Scaffolds,” J. Electrochem. Soc., 163(2), p. F54.

[20] Dowd, R. P., Lee, S., Fan, Y., and Gerdes, K., 2016, “Engineering the Solid Oxide Fuel Cell Electrocatalyst Infiltration Technique for Industrial Use,” International Journal of Hydrogen Energy, 41(33), pp. 14971–14981.

[21] Fan, H., Zhang, Y., and Han, M., 2017, “Infiltration of $La_{0.6}Sr_{0.4}FeO_{3-\delta}$ Nanoparticles into YSZ Scaffold for Solid Oxide Fuel Cell and Solid Oxide Electrolysis Cell,” Journal of Alloys and Compounds, 723, pp. 620–626.

[22] Zhang, P., Tong, J., and Huang, K., 2019, “Role of CO_2 in Catalytic Ethane-to-Ethylene Conversion Using a High-Temperature CO_2 Transport Membrane Reactor,” ACS Sustainable Chem. Eng., 7(7), pp. 6889–6897.

[23] Tanim, T., Bayless, D. J., and Trembly, J. P., 2014, “Modeling a 5 KWe Planar Solid Oxide Fuel Cell Based System Operating on JP-8 Fuel and a Comparison with Tubular Cell Based System for Auxiliary and Mobile Power Applications,” Journal of Power Sources, 245, pp. 986–997.

[24] Tanim, T., Bayless, D. J., and Trembly, J. P., 2013, “Modeling of a 5 KWe Tubular Solid Oxide Fuel Cell Based System Operating on Desulfurized JP-8 Fuel for Auxiliary and Mobile Power Applications,” Journal of Power Sources, 221, pp. 387–396.

[25] “Carbon Dioxide Utilization,” netl.doe.gov [Online]. Available: https://www.netl.doe.gov/LCA/CO2U. [Accessed: 31-Aug-2022].

[26] Buchheit, K., Noring, A., Lyengar, A., and Hackett, G., 2022, “Solid Oxide Cell and Stack Manufacturing Cost Tool.”

[27] Scataglini, R., Mayyas, A., Wei, M., Chan, S. H., Lipman, T., Gosselin, D., D’Alessio, A., Breunig, H., and Colella, W. G., “A Total Cost of Ownership Model for Solid Oxide Fuel Cells in Combined Heat and Power and Power-Only Applications,” p. 197.

[28] Chu, Y.-H., and He, X., "Process Simulation and Cost Evaluation of Carbon Membranes for CO_2 Removal from High-Pressure Natural Gas", 2018, Membranes (Basel), 8(4).